

Accelerated Article Preview

Io's tidal response precludes a shallow magma ocean

Received: 19 June 2024

Accepted: 21 November 2024

Accelerated Article Preview



Cite this article as: Park, R. S. et al. Io's tidal response precludes a shallow magma ocean. *Nature* <https://doi.org/10.1038/s41586-024-08442-5> (2024)

R. S. Park, R. A. Jacobson, L. Gomez Casajus, F. Nimmo, A. I. Ermakov, J. T. Keane, W. B. McKinnon, D. J. Stevenson, R. Akiba, B. Idini, D. R. Buccino, A. Magnanini, M. Parisi, P. Tortora, M. Zannoni, A. Mura, D. Durante, L. Iess, J. E. P. Connerney, S. M. Levin & S. J. Bolton

This is a PDF file of a peer-reviewed paper that has been accepted for publication. Although unedited, the content has been subjected to preliminary formatting. *Nature* is providing this early version of the typeset paper as a service to our authors and readers. The text and figures will undergo copyediting and a proof review before the paper is published in its final form. Please note that during the production process errors may be discovered which could affect the content, and all legal disclaimers apply.

1 Io's tidal response precludes a shallow magma ocean

2
3 R. S. Park¹, R. A. Jacobson¹, L. Gomez Casajus², F. Nimmo³, A. I. Ermakov⁴, J. T. Keane¹, W. B. McKinnon⁵,
4 D. J. Stevenson⁶, R. Akiba³, B. Idini³, D. R. Buccino¹, A. Magnanini⁷, M. Parisi¹, P. Tortora⁷, M. Zannoni⁷,
5 A. Mura⁸, D. Durante⁹, L. Iess⁹, J. E. P. Connerney¹⁰, S. M. Levin¹, and S. J. Bolton¹¹

6 1. Jet Propulsion Laboratory, California Institute of Technology, Pasadena, California, USA

7 2. Centro Interdipartimentale di Ricerca Industriale Aerospaziale, Alma Mater Studiorum - Università di Bologna, Forlì, Italy

8 3. Department of Earth and Planetary Sciences, University of California, Santa Cruz, California, USA

9 4. Department of Aeronautics and Astronautics, Stanford University, Stanford, California, USA

10 5. Department of Earth, Environmental, and Planetary Sciences, Washington University, St. Louis, Missouri, USA

11 6. California Institute of Technology, Pasadena, California, USA

12 7. Dipartimento di Ingegneria Industriale, Alma Mater Studiorum, Università di Bologna, Forlì, Italy

13 8. Institute for Space Astrophysics and Planetology, National Institute for Astrophysics, 00133 Rome, Italy

14 9. Sapienza Università di Roma, 00184 Rome, Italy.

15 10. NASA Goddard Space Flight Center, Greenbelt, Maryland, USA

16 11. Southwest Research Institute, San Antonio, Texas, USA

17 Corresponding author: Ryan.S.Park@jpl.nasa.gov

18 Copyright 2024. All rights reserved.

19 Abstract

20 Io experiences tidal deformation due to its eccentric orbit around Jupiter, which provides a primary energy source for Io's
21 ongoing volcanic activity and infrared emission¹. The amount of tidal energy dissipated within Io is enormous and has been
22 hypothesized to support the large-scale melting of Io's interior and the formation of a global subsurface magma ocean. If Io
23 has a shallow global magma ocean, its tidal deformation would be much larger than in the case of a more rigid, mostly solid
24 interior². Here we report the measurement of Io's tidal deformation, quantified by the gravitational tidal Love number k_2 ,
25 enabled by two recent flybys of the Juno spacecraft. By combining Juno^{3,4} and Galileo⁵⁻⁷ Doppler data from the Deep Space
26 Network and astrometric observations, we recover $\text{Re}(k_2)$ of 0.125 ± 0.047 (1σ) and the tidal dissipation parameter Q of 11.4 ± 3.6
27 (1σ). These measurements confirm that a shallow global magma ocean in Io does not exist and are consistent with Io having a
28 mostly solid mantle². Our results indicate that tidal forces do not universally create global magma oceans, which may be
29 prevented from forming due to rapid melt ascent, intrusion, and eruption^{8,9}, so even strong tidal heating – like that expected on
30 several known exoplanets and super-Earths¹⁰ – may not guarantee the formation of magma oceans on moons or planetary
31 bodies.

35 **Introduction**

36 Io is the innermost Galilean moon, orbiting Jupiter every 42.5 hours. It has a mean diameter of 3,643 km and a bulk density of
37 3,528 kg/m³, making it about 5% larger in both diameter and density than the Moon^{7,11}. Due to Io's eccentric orbit, its distance
38 from Jupiter varies by about 3,500 km, leading to variations in Jupiter's gravitational pull. Similar to tides on the Moon raised
39 by Earth, these gravitational variations cause tidal deformation on Io, which is theorized to serve as the primary energy source
40 for the intense volcanic activity and infrared emission observed on Io's surface^{1,12}.

41 The amount of energy dissipated within Io is immense with total power output around 100 TW¹³. For decades, it has been
42 speculated that this extreme tidal heating may be sufficient to melt a substantial fraction of Io's interior, plausibly forming a
43 global subsurface magma ocean. Many worlds are believed to have possessed magma oceans early in their evolution — notably
44 the early Moon, which is thought to have had a shallow magma ocean in the first 100 Myr caused by the giant impact which
45 birthed the body¹⁴. Io's extreme volcanism strongly suggests the existence of at least a partially molten interior. Whether the
46 interior contains a shallow global magma ocean has been an outstanding question since the discovery of Io's volcanism¹⁵.

47 Melt is expected to migrate rapidly from such partially-molten regions in the mantle^{8,9,16}; whether it accumulates to form a
48 magma ocean or simply erupts depends on many poorly-understood properties, including the nature of the melt pathways, the
49 melt volatile content, and Io's crustal density. Thus, there are two end-member models for Io's interior: a partially molten but
50 mostly solid interior, or an interior with a global magma ocean. A metallic core is also indicated from earlier gravitational
51 measurements, and is likely liquid⁷.

52 The existence of a global magma ocean has been predicted by two types of analysis. Magnetic induction measurements from
53 the Galileo mission suggested the existence of a magma ocean within Io hypothesizing an approximately 50-km thick near-
54 surface layer with >20% melt¹⁷ — although the results have been the subject of substantial debate¹⁸⁻²⁰. Recently, the global
55 mapping of Io's volcanoes by Juno was used to suggest that the distribution of volcanic heat flow is consistent with the presence
56 of a global magma ocean²¹, although, there is recent debate whether this technique can be used to distinguish whether Io's
57 volcanic activity is driven by a shallow global magma ocean²².

58 A measurement of Io's tidal response is a key diagnostic for distinguishing whether Io has a global magma ocean or not. If Io
59 does (not) have a magma ocean, the tidal response will be large (small)². Io's tidal response can be quantified by a complex
60 number called the gravitational tidal Love number²³ $k_2 = \text{Re}(k_2) + i\text{Im}(k_2)$. The real component $\text{Re}(k_2)$ characterizes the in-phase
61 response, defined as the ratio of the imposed gravitational potential from Jupiter to the induced potential from the deformation
62 of Io (see Methods). The out-of-phase part of the tidal response $\text{Im}(k_2)$ is often defined as $-|k_2|/Q$, where Q is the dissipation
63 quality factor, and is a measure of how much tidal heat Io should be generating. Previous studies have used astrometric
64 measurements to determine $|k_2|/Q$, but could not determine $\text{Re}(k_2)$ independently²⁴.

65 **Measuring Io's tidal response**

66 The Juno spacecraft has been exploring the Jovian system since mid-2016²⁵. By accurately tracking the motion of a spacecraft,
67 the gravity field of a perturbing body can be recovered^{26,27}. As of June 2024, Juno has completed a total of 62 orbits around
68 Jupiter, and the data acquired during this period have been used to improve our understanding of the dynamical environment
69 at Jupiter, especially the orbits of the Galilean satellites and Jupiter's gravity field and orientation^{3,4,28,29}. The two flybys directly
70 relevant for characterizing Io's tidal response are denoted I57 and I58, occurred on December 30, 2023, and February 3, 2024,
71 respectively (see Extended Data Fig. 1). I57 provided a unique opportunity to acquire the gravity data for Io's high northern
72 hemisphere. Two flybys of Io were designed as part of Juno's extended mission to investigate and determine whether a global
73 magma ocean exists in Io. Both flybys occurred at altitudes of about 1,500 km and provided close-proximity Doppler data, with
74 an order of magnitude greater accuracy than the Galileo Doppler data (see Extended Data Fig. 2). Combining the Juno data
75 with the previously acquired Galileo data⁷ and astrometric observations²⁴, we have recovered $\text{Re}(k_2) = 0.125 \pm 0.047$ (1 σ) and
76 $Q = 11.4 \pm 3.6$ (1 σ), yielding $|k_2|/Q = -\text{Im}(k_2) = 0.0109 \pm 0.0054$ (1 σ) (see Extended Data Table 1). In our model, the tides in Jupiter
77 due to Galilean satellites are assumed to have a constant time lag, and our recovered estimate is 0.11693 ± 0.00069 s (1 σ).
78 Moreover, the recovered J_2 and C_{22} for Io, including permanent tides, were $(1834.6 \pm 1.5) \times 10^6$ (1 σ) and
79 $(549.6 \pm 0.3) \times 10^6$ (1 σ), respectively, yielding the C_{22}/J_2 ratio of 0.2996 ± 0.0003 (1 σ), consistent with the 0.3 expected for
80 hydrostatic Io^{5,7,30}.

81 **Tidal Response Modeling**

82 Fig. 1 compares the Juno measurements (shaded green box) with simple Io models both without (Fig. 1a) and with (Fig. 1b) a
83 magma ocean (see Extended Data Table 2). These models use a viscoelastic (Andrade) rheology where the β parameter
84 describes the amplitude of the anelastic deformation and is expected to be in the range 10^{-13} – 10^{-10} Pa⁻¹ s⁻ⁿ for partially-molten
85 silicates³¹, and n describes the time-dependence of anelastic deformation. The effect of adding a magma ocean is most easily

seen by comparing the two cases where the elastic lid thickness (d , Fig. 1a) or upper mantle thickness (h , Fig. 1b) is 50 km. Without a magma ocean, $\text{Re}(k_2)$ can be as small as about 0.1, at which point the measured $|k_2|/Q$ value is also satisfied; with a magma ocean, $\text{Re}(k_2)$ is never less than 0.8 when $h=50$ km because the decoupling effect of the liquid layer leads to a larger tidal response. These results provide strong evidence demonstrating a shallow global subsurface magma ocean capable of being the source of Io's volcanic activity does not exist and are insensitive to the details of the rheology assumed because they arise from the mechanical decoupling effect of a liquid layer.

A thicker viscoelastic upper mantle overlying the magma ocean will reduce the surface deformation. Fig. 1b shows that an upper mantle 250-km thick (orange line) reduces $\text{Re}(k_2)$, but not by enough to satisfy the Juno measurement. However, an upper mantle with a thickness of approximately 500 km (purple line) can reproduce both the measured $\text{Re}(k_2)$ and $|k_2|/Q$. We confirm this result by conducting a comprehensive Markov chain Monte-Carlo (MCMC) study of Io's internal structure using k_2 and degree-2 gravity coefficients (see Extended Data Table 1) as observations for the cases with and without a magma ocean (see Methods). Our full model input is given in Extended Data Table 3 for the magma ocean case and Extended Data Table 4 for the no magma ocean case. For the case with a magma ocean beneath a viscoelastic (Andrade) mantle, our result shows that the thickness of the mantle must be greater than 318 km (at a 3σ level, see Extended Data Fig. 4a). Full posterior distributions with and without a magma ocean are shown in Extended Data Fig. 5 and Extended Data Fig. 6, respectively. The Juno results do not exclude the possibility of a deep magma ocean existing at a depth of >318 km, although a deep magma ocean could not be the source of Io's volcanic activity and we suggest such a deep magma ocean would resemble more the hypothesized basal magma ocean on Earth³², and perhaps Mars³³, rather than a shallow, Moon-like magma ocean³⁴. In addition, adding a surface elastic layer to the magma-ocean-bearing models does not change our conclusions (see Extended Data Fig. 3b in Methods).

A very thin (< 2 km), shallow magma ocean might produce a small $\text{Re}(k_2)$ consistent with our observations³⁵. However, Io's long-wavelength surface topography has amplitudes of about 1 km³⁶ and isostatic variations in the lid thickness will result in basal topography of at least a few kilometers, depending on the density contrast. We suggest for a very thin magma ocean, grounding would likely occur, and the magma ocean would no longer be global. We conclude that a shallow, global magma ocean is excluded by the Juno results and Fig. 2 presents an artistic illustration of Io's interior based on our results.

Because a deep global magma ocean is expected to mechanically decouple the crust, we explore the potential for measurements of diurnal librations of the surface to provide additional constraints. Our MCMC analysis (see Methods) shows that the posterior probability distributions of the libration amplitudes for cases with and without a magma ocean have a significant overlap (see Extended Data Fig. 4b and Extended Data Fig. 7). For a no magma ocean case, the libration amplitude ranges from 250 to 268 m (5%–95% confidence interval). For the magma ocean scenario, the libration amplitude could be larger, ranging from 261 to 317 m. Both values are at the lower end of the past predictions³⁷ due to the observed low value of $\text{Re}(k_2)$ from this study that requires a thick outer shell.

Magnetic induction has been suggested as another method to determine whether Io has a global magma ocean¹⁷. However, detecting a deep magma ocean using a magnetic induction technique may be challenging due to saturation at a relatively low melt fraction³⁸. The geometric tidal Love number, h_2 , also provides constraints on the tidal response; however, similar to k_2 , we expect this measurement would also be unable to discriminate between basal magma ocean and no magma ocean cases. Other measurements, such as obliquity, precession, nutation, and high-resolution gravity field, could also contribute to probing Io's deeper interior.

Io's lack of a shallow magma ocean

Our results indicate that a shallow global magma ocean in Io does not exist, and these findings are supported by our current knowledge of Io's long-wavelength shape³⁹. On Earth, deep melts can be denser than the surrounding mantle and thus remain sequestered in a basal magma ocean⁴⁰. On Io, pressures are much lower, so mantle melts are expected to be always less dense than the surrounding solid mantle. The melts will tend to ascend, making maintenance of a deep magma ocean dynamically problematic. Conversely, if the melts are dense (e.g., if sufficiently iron-rich), while a deep magma ocean could then form, it would be hard to explain how any such melt would ascend and erupt. Thus, we conclude that the volcanism seen on Io's surface is not sourced from a global magma ocean. While we cannot exclude a heterogeneous mantle⁴¹ in which both deep, dense melts and buoyant erupting magmas are present, no current observations support the existence of a deep molten layer.

How did the early Moon retain a shallow magma ocean for a relatively extended period¹⁴, whereas Io, which is continually tidally heated, does not? Two possibilities are a relative absence of volatiles on the Moon to drive eruptions, or the presence of the low-density anorthositic crust, which impedes upwards melt migration and eruption⁴². While Io's crustal thickness and structure are uncertain^{43,44}, volatile-driven eruptions are common⁴⁵. The Moon's magma ocean originated as a result of its

142 formation by a giant impact; in the absence of such a catastrophic event, tidal heating alone appears insufficient to allow such
143 a magma ocean to develop at Io.

144 Understanding tidal heating is important as a primary cause of oceans within our solar system, such as those on Europa and
145 Enceladus⁴⁶, and potentially beyond. Although it is commonly assumed among the exoplanet community that intense tidal
146 heating may lead to magma oceans^{10,47-49}, the example of Io shows that this need not be the case. Arguments that imply that
147 Vesta or other very-early-accreted asteroids or asteroidal parent bodies formed magma oceans from ²⁶Al decay heating may
148 also need to be reexamined^{50,51}. Rapid melt migration and eruption may frustrate the development of magma oceans⁸, unless
149 there exists a barrier to upwards motion. Such barriers likely existed for the early Moon, and also for icy satellites, where the
150 “melt” (water) is denser than the “crust” (ice) and oceans are common⁴⁶. Neither intense surficial silicate volcanism nor extreme
151 tidal heating necessarily imply a shallow magma ocean.

152 **References**

153 1 Peale, S. J., Cassen, P. & Reynolds, R. T. Melting of Io by Tidal Dissipation. *Science* **203**, 892-894 (1979).
<https://doi.org/10.1126/science.203.4383.892>

154 2 Bierson, C. J. & Nimmo, F. A test for Io's magma ocean: Modeling tidal dissipation with a partially molten mantle. *J Geophys Res-Planet* **121**, 2211-2224 (2016). <https://doi.org/10.1002/2016je005005>

155 3 Folkner, W. M. *et al.* Jupiter gravity field estimated from the first two Juno orbits. *Geophys Res Lett* **44**, 4694-4700 (2017). <https://doi.org/10.1002/2017gl073140>

156 4 Iess, L. *et al.* Measurement of Jupiter's asymmetric gravity field. *Nature* **555**, 220-+ (2018).
<https://doi.org/10.1038/nature25776>

157 5 Anderson, J. D., Jacobson, R. A., Lau, E. L., Moore, W. B. & Schubert, G. Io's gravity field and interior structure. *J Geophys Res-Planet* **106**, 32963-32969 (2001). <https://doi.org/10.1029/2000je001367>

158 6 Anderson, J. D., Sjogren, W. L. & Schubert, G. Galileo gravity results and the internal structure of Io. *Science* **272**, 709-712 (1996). <https://doi.org/10.1126/science.272.5262.709>

159 7 Schubert, G., Anderson, J. D., Spohn, T. & McKinnon, W. B. *Interior composition, structure and dynamics of the Galilean satellites*. (Cambridge Univ. Press, 2004).

160 8 Miyazaki, Y. & Stevenson, D. J. A Subsurface Magma Ocean on Io: Exploring the Steady State of Partially Molten Planetary Bodies. *Planet Sci J* **3** (2022). <https://doi.org/10.3847/PSJ/ac9cd1>

161 9 Moore, W. B. The thermal state of Io. *Icarus* **154**, 548-550 (2001). <https://doi.org/10.1006/icar.2001.6739>

162 10 Seligman, D. Z. *et al.* Potential Melting of Extrasolar Planets by Tidal Dissipation. *Astrophys J* **961** (2024).
<https://doi.org/10.3847/1538-4357/ad0b82>

163 11 Zuber, M. T. *et al.* Gravity Field of the Moon from the Gravity Recovery and Interior Laboratory (GRAIL) Mission. *Science* **339**, 668-671 (2013). <https://doi.org/10.1126/science.1231507>

164 12 Keane, J. T., Matsuyama, I., Bierson, C. J. & Trinh, A. in *Io: A New View of Jupiter's Moon* (eds Rosaly M. C. Lopes, Katherine de Kleer, & James Tuttle Keane) 95-146 (Springer International Publishing, 2023).

165 13 Veeder, G. J., Matson, D. L., Johnson, T. V., Blaney, D. L. & Goguen, J. D. Io's heat flow from infrared radiometry: 1983-1993. *Journal of Geophysical Research: Planets* **99**, 17095-17162 (1994). <https://doi.org/10.1029/94JE00637>

166 14 Maurice, M., Tosi, N., Schwinger, S., Breuer, D. & Kleine, T. A long-lived magma ocean on a young Moon. *Sci Adv* **6** (2020). <https://doi.org/10.1126/sciadv.aba8949>

167 15 de Kleer, K., McEwen, A. S. & Park, R. S. Tidal Heating: Lessons from Io and the Jovian System, Final Report for the Keck Institute for Space Studies. (2019).

168 16 Monnereau, M. & Dubuffet, F. Is Io's mantle really molten? *Icarus* **158**, 450-459 (2002).
<https://doi.org/10.1006/icar.2002.6868>

169 17 Khurana, K. K. *et al.* Evidence of a Global Magma Ocean in Io's Interior. *Science* **332**, 1186-1189 (2011).
<https://doi.org/10.1126/science.1201425>

170 18 Blöcker, A., Saur, J., Roth, L. & Strobel, D. F. MHD Modeling of the Plasma Interaction With Io's Asymmetric Atmosphere. *Journal of Geophysical Research: Space Physics* **123**, 9286-9311 (2018).
<https://doi.org/10.1029/2018JA025747>

171 19 Roth, L. *et al.* Constraints on Io's interior from auroral spot oscillations. *Journal of Geophysical Research: Space Physics* **122**, 1903-1927 (2017). <https://doi.org/10.1002/2016JA023701>

172 20 Šebek, O., Trávníček, P. M., Walker, R. J. & Hellinger, P. Dynamic Plasma Interaction at Io: Multispecies Hybrid Simulations. *Journal of Geophysical Research: Space Physics* **124**, 313-341 (2019).
<https://doi.org/10.1029/2018JA026153>

173 21 Davies, A. G., Perry, J. E., Williams, D. A. & Nelson, D. M. Io's polar volcanic thermal emission indicative of magma ocean and shallow tidal heating models (8, pg 94, 2024). *Nat Astron* **8**, 397-397 (2024).
<https://doi.org/10.1038/s41550-023-02182-8>

174 22 Pettine, M. *et al.* JIRAM Observations of Volcanic Flux on Io: Distribution and Comparison to Tidal Heat Flow Models. *Geophys Res Lett* **51**, e2023GL105782 (2024). <https://doi.org/10.1029/2023GL105782>

175 23 Efroimsky, M. & Lainey, V. Physics of bodily tides in terrestrial planets and the appropriate scales of dynamical evolution. *J Geophys Res-Planet* **112** (2007). <https://doi.org/10.1029/2007je002908>

176 24 Lainey, V., Arlot, J. E., Karatekin, Ö. & Van Hoolst, T. Strong tidal dissipation in Io and Jupiter from astrometric observations. *Nature* **459**, 957-959 (2009). <https://doi.org/10.1038/nature08108>

177 25 Bolton, S. J. *et al.* The Juno Mission. *Space Sci Rev* **213**, 5-37 (2017). <https://doi.org/10.1007/s11214-017-0429-6>

178 26 Asmar, S. W. *et al.* The Juno Gravity Science Instrument. *Space Sci Rev* **213**, 205-218 (2017).
<https://doi.org/10.1007/s11214-017-0428-7>

179 27 Park, R. S. *et al.* A partially differentiated interior for (1) Ceres deduced from its gravity field and shape. *Nature* **537**, 515-517 (2016). <https://doi.org/10.1038/nature18955>

180 28 Durante, D. *et al.* Jupiter's Gravity Field Halfway Through the Juno Mission. *Geophys Res Lett* **47** (2020).
<https://doi.org/10.1029/2019GL086572>

210 29 Kaspi, Y. *et al.* Observational evidence for cylindrically oriented zonal flows on Jupiter. *Nat Astron* (2023).
<https://doi.org/10.1038/s41550-023-02077-8>

211 30 Tricarico, P. Multi-layer hydrostatic equilibrium of planets and synchronous moons: theory and application to Ceres and to solar system moons. *The Astrophysical Journal* **782**, 99 (2014). <https://doi.org/10.1088/0004-637X/782/2/99>

212 31 Jackson, I., Faul, U. H., Gerald, J. D. F. & Tan, B. H. Shear wave attenuation and dispersion in melt-bearing olivine polycrystals: 1. Specimen fabrication and mechanical testing. *J Geophys Res-Sol Ea* **109** (2004).
<https://doi.org/10.1029/2003jb002406>

213 32 Labrosse, S., Hernlund, J. W. & Coltice, N. A crystallizing dense magma ocean at the base of the Earth's mantle. *Nature* **450**, 866-869 (2007). <https://doi.org/10.1038/nature06355>

214 33 Khan, A. *et al.* Evidence for a liquid silicate layer atop the Martian core. *Nature* **622**, 718-723 (2023).
<https://doi.org/10.1038/s41586-023-06586-4>

215 34 Elkins-Tanton, L. T., Burgess, S. & Yin, Q. Z. The lunar magma ocean: Reconciling the solidification process with lunar petrology and geochronology. *Earth Planet Sc Lett* **304**, 326-336 (2011).
<https://doi.org/10.1016/j.epsl.2011.02.004>

216 35 Aygün, B. & Čadek, O. Tidal Heating in a Subsurface Magma Ocean on Io Revisited. *Geophys Res Lett* **51**, e2023GL107869 (2024). <https://doi.org/https://doi.org/10.1029/2023GL107869>

217 36 White, O. L., Schenk, P. M., Nimmo, F. & Hoogenboom, T. A new stereo topographic map of Io: Implications for geology from global to local scales. *J Geophys Res-Planet* **119**, 1276-1301 (2014).
<https://doi.org/10.1002/2013je004591>

218 37 Van Hoolst, T., Baland, R. M., Trinh, A., Yseboodt, M. & Nimmo, F. The Librations, Tides, and Interior Structure of Io. *J Geophys Res-Planet* **125** (2020). <https://doi.org/10.1029/2020JE006473>

219 38 Schilling, F. R., Partzsch, G. M., Brasse, H. & Schwarz, G. Partial melting below the magmatic arc in the central Andes deduced from geoelectromagnetic field experiments and laboratory data. *Phys Earth Planet In* **103**, 17-31 (1997). [https://doi.org/10.1016/S0031-9201\(97\)00011-3](https://doi.org/10.1016/S0031-9201(97)00011-3)

220 39 Gyalay, S. & Nimmo, F. Io's Long-Wavelength Topography as a Probe for a Subsurface Magma Ocean. *Geophys Res Lett* **51**, e2023GL106993 (2024). <https://doi.org/10.1029/2023GL106993>

221 40 Mosenfelder, J. L., Asimow, P. D. & Ahrens, T. J. Thermodynamic properties of MgSiO liquid at ultra-high pressures from shock measurements to 200 GPa on forsterite and wadsleyite. *J Geophys Res-Sol Ea* **112** (2007).
<https://doi.org/10.1029/2006jb004364>

222 41 Keszthelyi, L. P. & Suer, T.-A. in *Io: A New View of Jupiter's Moon* (eds Rosaly M. C. Lopes, Katherine de Kleer, & James Tuttle Keane) 211-232 (Springer International Publishing, 2023).

223 42 Wilson, L. & Head, J. W. Generation, ascent and eruption of magma on the Moon: New insights into source depths, magma supply, intrusions and effusive/explosive eruptions (Part 1: Theory). *Icarus* **283**, 146-175 (2017).
<https://doi.org/10.1016/j.icarus.2015.12.039>

224 43 Keszthelyi, L. & McEwen, A. Magmatic differentiation of Io. *Icarus* **130**, 437-448 (1997).
<https://doi.org/10.1006/icar.1997.5837>

225 44 Leone, G. & Wilson, L. Density structure of Io and the migration of magma through its lithosphere. *J Geophys Res-Planet* **106**, 32983-32995 (2001). <https://doi.org/10.1029/2000je001379>

226 45 Cataldo, E., Wilson, L., Lane, S. & Gilbert, J. A model for large-scale volcanic plumes on Io: Implications for eruption rates and interactions between magmas and near-surface volatiles. *J Geophys Res-Planet* **107** (2002).
<https://doi.org/10.1029/2001je001513>

227 46 Nimmo, F. & Pappalardo, R. T. Ocean worlds in the outer solar system. *J Geophys Res-Planet* **121**, 1378-1399 (2016). <https://doi.org/10.1002/2016je005081>

228 47 Barr, A. C., Dobos, V. & Kiss, L. L. Interior structures and tidal heating in the TRAPPIST-1 planets. *Astron Astrophys* **613** (2018). <https://doi.org/10.1051/0004-6361/201731992>

229 48 Driscoll, P. E. & Barnes, R. Tidal Heating of Earth-like Exoplanets around M Stars: Thermal, Magnetic, and Orbital Evolutions. *Astrobiology* **15**, 739-760 (2015). <https://doi.org/10.1089/ast.2015.1325>

230 49 Walterová, M. & Behounková, M. Thermal and Orbital Evolution of Low-mass Exoplanets. *Astrophys J* **900** (2020).
<https://doi.org/10.3847/1538-4357/aba8a5>

231 50 Neumann, W., Breuer, D. & Spohn, T. Differentiation of Vesta: Implications for a shallow magma ocean. *Earth Planet Sc Lett* **395**, 267-280 (2014). <https://doi.org/10.1016/j.epsl.2014.03.033>

232 51 Scherstén, A., Elliott, T., Hawkesworth, C., Russell, S. & Masarik, J. Hf-W evidence for rapid differentiation of iron meteorite parent bodies. *Earth Planet Sc Lett* **241**, 530-542 (2006). <https://doi.org/10.1016/j.epsl.2005.11.025>

263
264
265

Main figure legends

266 **Fig. 1 | The measured tidal response ($Re(k_2)$ and $|k_2|/Q$) of Io compared against models without and with a magma**
267 **ocean.** a) No magma ocean. Shaded green boxes are 1σ and 3σ Juno results (see Methods) and shaded grey boxes are from a
268 previous study based on astrometry²⁴. Here a 3-layer Io is assumed with an elastic lid of thickness d , a partially-molten
269 mantle with an Andrade parameter β (in $\text{Pa}^{-1} \text{ s}^{-n}$) as specified by the symbols, and a liquid iron core. The second Andrade
270 parameter is assumed to be $n=0.3$. The purple star marker represents the model from Fig. 2 of Bierson & Nimmo². b) As for
271 a), but for models including a magma ocean with upper mantle. Here the ocean is at a depth h and is sandwiched between two
272 Andrade viscoelastic layers. The magma ocean is assumed to be 100-km thick. Increasing the upper mantle thickness reduces
273 $Re(k_2)$, as expected; to match the Juno results, the depth h exceeds 500 km which correlates to a deep magma ocean. Further
274 details are given in the Methods section.
275
276

277 **Fig. 2 | The internal structure of Io as revealed by the present study.** Our estimate of k_2 suggests that Io does not have a
278 shallow global magma ocean and is consistent with that expected for a mostly solid mantle (green hues), with substantial melt
279 (yellows and oranges), overlying a liquid core (red/black). Artist rendering by Sofia Shen (JPL / Caltech).

280
281
282
283
284
285
286
287
288
289

Methods

Data set

283 The dataset used in this study includes the Deep Space Network (DSN) radiometric data acquired during the Io flybys of
284 the Juno^{3,4} and Galileo⁵⁻⁷ spacecraft, as well as astrometric observations²⁴. The primary Juno data consist of simultaneous
285 two-way X-band (8.4 GHz) and Ka-band (32 GHz) data, referenced to X-band uplink, during I57 (December 30, 2023) and
286 I58 (February 3, 2024). Both flybys occurred at an altitude of approximately 1500 km with a relative velocity of about 30
287 km/s. I57 was the only close approach in the high northern hemisphere, which was particularly helpful for acquiring
288 improved global coverage of gravity data.
289

290 The primary Galileo data consist of the S-band (2.3 GHz) two-way Doppler data acquired during five flybys: I24, I25, I27,
291 I32 and I33 at lower signal-to-noise ratio than Juno's measurements due to the Galileo's High Gain Antenna deployment
292 anomaly. Details on Galileo flybys can be found in Schubert et al. (2004) and discussions on the astrometric data set used in
293 this study can be found in Lainey et al. (2009). The ground tracks and flyby altitudes of Galileo and Juno are shown in
294 Extended Data Fig. 1 for the altitude \leq 5,000 km of the closest approach over a color image mosaic of Io⁵². The flybys sample
295 different true anomalies, latitudes, and longitudes, providing good coverage for measuring the long-wavelength
296 gravitational signature of Io.
297

Data calibration

298 The Doppler data between DSN and spacecraft are affected by the media in between. The Earth troposphere and ionosphere
299 effects are calibrated using a standard method⁵³. Additionally, the Doppler data were calibrated for the path delay due to the Io
300 plasma torus (IPT), a region of plasma generated by the ionization of the particles ejected by Io's volcanic activity⁵⁴.
301

302 For Juno I57 and I58 data, using the dual-frequency X- and Ka-band data with the primary data set being X-up/X-down and
303 X-up/Ka-down during the closest approach, the IPT path delay due to dispersive sources was calibrated using the dual-
304 frequency downlink data. This calibration allowed for the direct extraction of the downlink leg Doppler shift caused by
305 dispersive media^{55,56}. Then, the contribution on the uplink leg was corrected by scaling the actual downlink contribution to
306 account for the different uplink carrier frequency (7.1 GHz).
307

308 The Galileo high-gain antenna failed to completely open, significantly reducing the signal to noise ratio for the Doppler
309 tracking. The Galileo Doppler noise was dominated by instrumental noise rather than the expected interplanetary plasma noise.
310 To calibrate Galileo Doppler data, the total electron density of the Io plasma torus has been integrated along the line-of-sight
311 of the spacecraft using parametric models of the electron density distribution in the Jovian environment. The accuracy of these
312 models is limited by the spatial and temporal variability of the IPT^{57,58}. We built electron density distribution models for the
313 warm torus for each Galileo flyby using the data acquired by the Plasma Wave Subsystem (PWS)⁵⁹ during the same flyby, thus,
314 using direct information about the electron density of the IPT at the moment of the Doppler measurements. The local electron
315 densities of the plasma extracted from the PWS data were projected into the centrifugal equator along the magnetic field lines
316 of the dipole model using a scale height function of the centrifugal equator distance and assuming longitudinal symmetry.
317 Subsequently, following Phipps et al. (2018)⁶⁰, the electron density was fitted with Gaussian functions. Since the only Galileo
318 flyby of Io that acquired PWS observations of the cold and ribbon tori was I00, during the Jupiter orbital insertion, two different
319 models were generated for each flyby. One used the cold and ribbon observations from I00 Galileo flyby and was applied in
320 I24, I25, and I27. The other one used the cold torus and ribbon shapes from Phipps et al. (2018), derived from Voyager data,
321 and it was applied in I32 and I33. The choice of the model was decided by evaluating its performance for each flyby. Finally,
322 the expected Doppler shift has been derived from the computed path delay and used to calibrate the data. The use of IPT-
323 calibrated observables resulted in roughly a factor of two improvement in the root-mean-square (rms) of the residuals.
324

325 The Doppler residuals of Galileo (I24, I25, I27, I32, and I33) and Juno (I57 and I58) are shown in Extended Data Fig. 2. Note
326 that the I57 noise was dominated by Earth's troposphere noise, whereas the I58 noise was dominated by plasma interactions.
327 In general, we weigh the data per DSN pass, and the data weights are further refined based on various simulations to ensure
328 our weighting scheme is robust. We note that some of the data points show non-Gaussian behavior, but we have a large enough
329 dataset to still perform a least-squares fit and rely on the Central Limit Theorem when interpreting the statistics. One key point
330 to note is that our results do not vary in a statistically significant way even if we remove the residual points exceeding or near
331 the 3- σ level.
332

333
334
335

336
337
338

339 **The gravity field of Io**

340 The gravitational potential, $U(r, \lambda, \phi)$, associated with Io is expressed as a spherical harmonic expansion^{27,61,62}:

341

$$U(r, \lambda, \phi) = \frac{\mu_i}{r} \sum_{l=0}^{\infty} \sum_{m=0}^l \left(\frac{R}{r}\right)^l P_{lm}(\sin \phi) [C_{lm} \cos(m\lambda) + S_{lm} \sin(m\lambda)] \quad (1)$$

342

343 where μ_i is the mass parameter of Io, l is the spherical harmonic degree, m is the order, P_{lm} are the un-normalized Associated
344 Legendre polynomials, C_{lm} and S_{lm} are the un-normalized spherical harmonic coefficients, R is the reference radius of Io
345 (1829.4 km), λ is longitude, ϕ is latitude, and r is the distance. The spherical coordinates (λ, ϕ, r) are evaluated at the spacecraft
346 position relative to the Io body-fixed frame. In this formulation zonal coefficients are defined as $J_l = -C_{l0}$. The gravity field is
347 modeled in an Io-body-fixed frame, where the body pole direction is aligned with its orbit-normal direction, and the body x -
348 axis is pointed along the Io-Jupiter direction at the periapsis. Io is in synchronous rotation, where the period of rotation matches
349 the orbital period. Since we are assuming that the origin of the Io body-fixed frame is defined to be Io's center of mass, the
350 degree-one coefficients are identically zero.

351

The effects of the tide raised on Io by Jupiter can be modeled as corrections to Io's gravitational harmonic coefficients⁶³⁻⁶⁶:

$$\Delta J_2 = |k_2| \left(\frac{\mu_j}{\mu_i}\right) \left(\frac{R}{r_{ij}}\right)^3 \left(\frac{1 - 3 \sin^2 \phi_j}{2}\right) \quad (2)$$

$$\Delta C_{21} - i\Delta S_{21} = |k_2| \left(\frac{\mu_j}{\mu_i}\right) \left(\frac{R}{r_{ij}}\right)^3 (\sin \phi_j \cos \phi_j) e^{-i(\lambda_j + \delta)} \quad (3)$$

$$\Delta C_{22} - i\Delta S_{22} = |k_2| \left(\frac{\mu_j}{\mu_i}\right) \left(\frac{R}{r_{ij}}\right)^3 \left(\frac{1 - \sin^2 \phi_j}{4}\right) e^{-2i(\lambda_j + \delta)} \quad (4)$$

352
353
354
355
356
357

where k_2 represents the degree-2 gravitational tidal Love number, μ_j represents the mass parameter of Jupiter, r_{ij} represents
the distance from Io to Jupiter, δ represents the tidal lag angle, λ_j and ϕ_j represent Io-fixed longitude and latitude of Jupiter,
respectively. These corrections vary with time as Io moves around Jupiter causing periodic variations in λ_j , ϕ_j , and r_{ij} . It is
important to note that the corrections have non-zero average values known as the 'permanent tide'. Extended Data Table 1
includes the permanent tide values determined based on our estimated $\text{Re}(k_2) = 0.125$ by averaging ΔJ_2 and ΔC_{22} over the
Galileo to Juno time period.

358
359
360
361
362
363
364

The determination of Io's gravitational coefficient, C_{22} , was made in 1996⁶. Because of the limited data from the single flyby,
only the single coefficient could be determined. Consequently, the hydrostatic equilibrium constraint was imposed by forcing
 J_2 to be exactly 10/3 of C_{22} . After the first Io flyby of the Galileo Millennium Mission (GMM) mission, Io's gravitational
quadrupole moments (second degree and order gravitational harmonics) were recovered from the data acquired during four
flybys of the prime, Galileo Europa Mission, and GMM missions⁵. The data set was sufficiently robust that the hydrostatic
constraint was unneeded and was omitted. After the completion of the GMM mission, the gravity analysis was extended by
adding the data from the final Io flyby⁷.

365
366
367
368
369
370
371
372
373
374

As with the previous published analyses, we found that there is no significant sensitivity in the data set to the gravity field of
degree higher than the quadrupole. Extended Data Table 1 shows our gravity results along with those previously published.
The C_{21} and S_{21} are related to the misalignment of the satellite's principal axes and body coordinate axes. Their small values
confirm that the two systems are nearly aligned. The small S_{22} value is primarily a consequence of the principal axis prime
meridian not quite matching our coordinate system prime meridian as defined by the sub-planet direction. We find the ratio of
our total C_{22} to our total J_2 is 0.2996 ± 0.0003 (1σ), nearly the 0.3 required for hydrostatic equilibrium³⁰. A truly hydrostatic
(fluid) Io could be subject to a slightly non-synchronous (or pseudo-synchronous) rotation due to the non-zero orbital average
of the diurnal tidal torque⁶⁷. The small S_{22} value, with the uncertainty consistent with zero, aligns with an offsetting torque due
to a permanent (or quasi-permanent, i.e., geologically ephemeral) non-hydrostatic mass distribution. This distribution stabilizes
Io in the 1:1 spin-orbit resonance, similar to what is observed for Earth's Moon⁶⁸.

375

376

377

Effect of Io's libration

The expected amplitude of Io's diurnal libration is about 275 m in the absence of a magma ocean³⁷. While with a magma ocean the diurnal libration of the crust can be much larger than these values, the detectability through radiometric data is limited to its solid interior, which should have low values³⁷. We implemented a libration model by imposing Io's prime meridian to point the instantaneous peri-focus of its orbit^{69,70}. Then, the forced physical libration at the orbital period is modeled as $\gamma = A \sin M$, where M represents the mean anomaly and A is the amplitude of the physical libration. Since the available data is not sensitive enough to detect the diurnal libration of Io, we assessed its effect in our analysis including different amplitudes of libration ranging from 10 to 500 meters. In all the cases, the estimated k_2 remained within 1σ of its nominal value, indicating that the recovery of k_2 is insensitive to Io's libration at the accuracy level of the recovered quadrupole moments.

386

387

The tides in the Jovian system

Tidal interaction is presumed to play a crucial role in the long-term evolution of the orbits of the Galilean satellites. Io's active volcanism and associated heat flow are driven by tidal dissipation within the satellite. It is of high interest to determine whether Io is spiraling into or away from Jupiter. If the former is true, Io is losing more energy through internal dissipation than it is gaining from the torque on the tidal bulge that it raises on Jupiter. The amount of the heat produced by tidal friction has a direct bearing on the thickness of its outer shell or lithosphere and the nature of the internal melt distribution, including the possibility of a subsurface magma ocean.

394

395

396

397

398

The tide model is based on the theory of equilibrium tides in which the gravitational attraction of a point mass distorts a spherical body resulting in a tidal bulge. The acceleration acting on body a due to a tidal bulge raised by body b on Jupiter is^{24,71}:

$$\mathbf{a}_a = \frac{3}{2} \mu_b \frac{|k_2^j|}{R_j^2} \left(\frac{R_j}{r_{aj}} \right)^4 \left(\frac{R_j}{r_{bj}^*} \right)^3 \left\{ \left[1 - 5(\hat{\mathbf{r}}_{aj} \cdot \hat{\mathbf{r}}_{bj}^*)^2 \right] \hat{\mathbf{r}}_{aj} + 2(\hat{\mathbf{r}}_{aj} \cdot \hat{\mathbf{r}}_{bj}^*) \hat{\mathbf{r}}_{bj}^* \right\} \quad (5)$$

399

400

401

402

403

404

where μ_b is the mass parameters (i.e., GM) of body b , k_2^j is the love number of Jupiter, R_j is the Jupiter radius, r_{aj} and r_{bj}^* are the respective distances between Jupiter and bodies a and b , and $\hat{\mathbf{r}}_{aj}$ and $\hat{\mathbf{r}}_{bj}^*$ are the respective directions from Jupiter to bodies a and b . Because Jupiter does not respond instantaneously to tide raising body b , the tidal bulge is offset from its current direction. We introduce this offset by assuming that there is simply a time delay Δt_b between when the tidal bulge is raised and when it acts on body a . Consequently, the relation between position vector \mathbf{r}_{bj}^* and the current position \mathbf{r}_{bj} is:

$$\mathbf{r}_{bj}^* = \mathbf{r}_{bj} - \Delta t_b (\dot{\mathbf{r}}_{bj} + \dot{W}_j (\mathbf{r}_{bj} \times \hat{\mathbf{h}}_j)) \quad (6)$$

405

406

407

408

409

410

where $\dot{\mathbf{r}}_{bj}$ is the velocity of body b relative to Jupiter, \dot{W}_j is the rotation rate of Jupiter, and $\hat{\mathbf{h}}_j$ is Jupiter's pole direction. More details can be found in previous studies^{23,24,72}.

The tidal time delay is related to the measure of the tidal dissipation, the tidal quality factor Q_b , through the lag angle δ_b :

$$\delta_b = \frac{\Delta t_b}{r_{bj}} |\dot{\mathbf{r}}_{bj} + \dot{W}_j (\mathbf{r}_{bj} \times \hat{\mathbf{h}}_j)| \quad (7)$$

411

412

413

414

415

416

417

418

The quality factor is related to the lag angle (δ_b) by $Q_b^{-1} = \tan 2\delta_b$. The relationship between the quality factor Q and k_2 is often represented as $\text{Im}(k_2) = -|k_2|/Q$.

For the case of a tide raised on a synchronously rotating satellite c by Jupiter, we consider only the self-tide (the effect on the satellite by the tide raised on it). We assume that the satellite pole is aligned with the orbit normal, $\hat{\mathbf{h}}_c$. Consequently, the acceleration due to the tide raised on a synchronously satellites is:

$$\mathbf{a}_c = -3|k_2^c| \left(\frac{\mu_j}{R_c^2} \right) \left(\frac{R_c}{r_{jc}} \right)^7 \left\{ \left[1 + 3\Delta t_c \frac{(\hat{\mathbf{r}}_{jc} \cdot \dot{\mathbf{r}}_{jc})}{r_{jc}} \right] \hat{\mathbf{r}}_{jc} + \Delta t_c (n_c - \dot{\theta}_c) (\hat{\mathbf{r}}_{jc} \times \hat{\mathbf{h}}_c) \right\} \quad (8)$$

419

420

421

422

where $\dot{\theta}_c$ is the satellite's instantaneous angular velocity and the satellite's rotation rate matches its mean orbital motion, i.e., $\dot{W}_c = n_c$. Specifically, we use the average rotation rate over the 100 years from 1950 to 2050 for the rotation rate, \dot{W}_c . The angular velocity is computed as the magnitude of the orbital angular momentum divided by the square of the radial distance.

423 The assumption is that the rotation rate will not vary significantly over a few hundred years, periodic variations due to librations
424 are small, and the tidal torque has nearly damped out. The delayed tidal force has a radial component proportional to the radial
425 velocity and a component perpendicular to the radial direction and proportional to the difference between the mean motion and
426 the instantaneous angular velocity. By convention, for satellites, we compute the quality factor Q_c from the lag angle $\delta_c =$
427 $\frac{1}{2}n_c\Delta t_c$. The gravitational effects of the bulges raised on Jupiter tend to move the satellites away from Jupiter, decreasing their
428 mean motions. The tidal bulge raised by Jupiter on Io has the opposite effect.
429

430 We numerically integrated the orbits of Galilean satellites with tide models and fit them to the spacecraft and astrometry data.
431 The models and estimated parameters for the Jupiter satellite ephemeris and gravity field are broadly similar to the work done
432 on the Saturnian system⁷³. The positions and masses of the Sun, Moon, and planets are from the JPL planetary ephemeris
433 DE440⁷⁴. Our estimated tidal time lag of Io is $\Delta t = 2129.6 \pm 677.0$ s (1 σ), which corresponds to $Q = 11.4 \pm 3.6$ (1 σ).
434 Combining k_2 and Q , we get $k_2/Q = -\text{Im}(k_2) = 0.0109 \pm 0.0054$ (1 σ), which is consistent with $k_2/Q = 0.015 \pm 0.003$ (1 σ) from
435 Lainey et al. (2009). We note that since Io's rotation rate is known with much higher accuracy, any meaningful error in the
436 rotation rate, both secular and periodic, would have a minimal effect within the uncertainty of the recovered Δt . In fact, a first-
437 order analysis suggests that if forced libration with an upper-end amplitude of the constraint based on our k_2 estimate were to
438 exist (see Extended Data Fig. 4), the resulting error in the time delay would only be at a few percent level, which is substantially
439 below the accuracy of the recovered tidal delay. Thus, although in theory it may be possible that the small angle effect would
440 potentially show up for a very long period, it is not significant for the relatively short time span considered in our study.
441 Furthermore, in our model, we assume the tides in Jupiter have a constant time lag. Our recovered estimate is 0.11693 ± 0.00069
442 s (1 σ), which corresponds to $Q_{\text{jupiter}} = 31733 \pm 188$ (1 σ) at the Io frequency and is consistent with previous results²⁴. We
443 also note that while k_2 is primarily determined from Juno and Galileo data, the Q values for both Io and Jupiter are primarily
444 determined from the long-term dynamics of the Galilean satellites via ground-based astrometry. In other words, k_2 and Q are
445 independently estimated and are not correlated.
446

447 **Interior modeling of Io**

448 Because of the large uncertainties in appropriate parameters to use, we adopt a simplified model for Io's structure. A more
449 complicated, self-consistent approach² yields essentially identical results (purple star marker in Fig. 1a). Based on Io's bulk
450 density and moment of inertia, we assume an iron/iron-sulfide core to have a radius of 950 km and a density of 5,150 kg m⁻³
451 and the mantle to have a density of 3,259 kg m⁻³ and an outer radius of 1,820 km⁷ (Extended Data Table 2). The core is assumed
452 to be liquid and the mantle to have an infinite-frequency shear modulus of 40 GPa, which is at the upper end of that expected
453 for partially-molten olivine. Lower shear moduli would make it more challenging to match the measured k_2 with a magma
454 ocean. Note that while constrained by static gravity field observations, there is some uncertainty about the composition and
455 size of the metallic core – which we do not explore here. But these uncertainties will have a small effect compared to the state
456 of the core (solid or liquid). Extended Data Fig. 3a shows that the difference between a solid and liquid core is minor; a solid
457 core reduces both $\text{Re}(k_2)$ and k_2/Q for the same mantle rheology (and the change for a partially liquid core would be smaller
458 still). In addition, we note that a silicate mantle at or above the solidus will exceed the melting point of any plausible Fe-FeS
459 core composition at core pressures⁷. Our baseline models assume a 100-km thick magma ocean (see below).

460 Our three-layer Io has a purely elastic lid (with thickness d) with a single viscoelastic mantle layer beneath, consistent with
461 expectations that for a heat-pipe body such as Io, there will be a cold and rigid near-surface layer⁷⁵. The four-layer model has
462 two viscoelastic layers, separated by a magma ocean (see Fig. 1). A purely elastic (as opposed to viscoelastic) top layer would
463 reduce $|k_2|/Q$ well below the measured value. The effect of adding a 50 km thick elastic lid to the magma ocean case (that is, a
464 five-layer model) is shown in Extended Data Fig. 3b. The effect is negligible at low $\text{Re}(k_2)$ values because in these cases the
465 primary resistance to tidal deformation is due to the mantle and not the lid.

466 The viscoelastic mantle is described by a single Andrade rheology, details of which may be found in Bierson & Nimmo (2016)².
467 We do not adopt a Maxwell model as it provides a poor description of the rheology of real geological materials³¹. We assume
468 that the Andrade parameter $n=0.3$ throughout and vary the β parameter as noted in Fig. 1. We take the mantle viscosity to be
469 10^{21} Pa s, but varying this value does not affect our results unless the viscosity chosen is $<10^{15}$ Pa s. In the Andrade model the
470 effective forcing frequency is related to the actual forcing frequency via an Arrhenius term which accounts for the changing
471 response as a function of temperature². We take this term to be 3.16, representing mantle material that is close to the melting
472 point.

473 Our baseline models all assumed a magma ocean thickness of 100 km and varied its depth. We also investigated the effect of
474 reducing the magma ocean thickness and found that a magma ocean 5 km and 2 km thick resulted in reductions in $\text{Re}(k_2)$ of
475 0.3% and 7.7%, respectively. Note that our models all neglect inertial terms and thus neglect the more complicated dynamics
476 treated in Tyler et al. (2015) or Aygun & Cadek (2024); in common with most models, they also neglect bulk dissipation⁷⁶.

477 For a given internal model of Io, the complex Love number k_2 is computed for the tidal response of a viscoelastic body
478 composed of solid and liquid layers^{77,78}. The forced libration amplitude of a given internal model of Io is computed using an
479 approach that includes viscoelastic Andrade rheology⁷⁹. The response of a viscoelastic layer relative to a fluid response is
480 described by the layer-wise tidal and fluid Love numbers, k_2^j and $k_{2,f}^j$, respectively. The fluid Love number $k_{2,f}^j$ describes a
481 layer within a body in hydrostatic equilibrium, found from the flattening factors computed for a multi-layered Io³⁰.

482 **MCMC internal structure retrieval**

483 We solve the inverse problem of constraining Io's internal structure using Markov-chain Monte Carlo (MCMC). We test two
484 internal structure models with and without a magma ocean. A large parameter space is explored using the affine invariant
485 ensemble sampler implemented in the open-source library, emcee⁸⁰. Our full model input is given by the vector of input
486 parameters given in Extended Data Table 3 for the magma ocean case and Extended Data Table 4 for the no magma ocean
487 case. Extended Data Tables 3 and 4 also show the parameters of the prior probability distribution for each parameter.

488 The MCMC sampler is then run to obtain layer thicknesses and densities as well as rheologic parameters, which are used to
489 generate synthetic observations of static gravity and complex valued Love number k_2 . The synthetic observation vector $\mathbf{X} =$
490 $[C_{20}, C_{22} \operatorname{Re}(k_2), \operatorname{Im}(k_2)]^T$ is compared to the observed values \mathbf{Y} and their covariance matrix Σ by computing the log-likelihood
491 function $\log L = -\frac{1}{2}(\mathbf{X} - \mathbf{Y})^T \Sigma^{-1} (\mathbf{X} - \mathbf{Y})$. The full covariance matrix can be constructed using the data provided in Extended
492 Data Table 1 assuming $\operatorname{Im}(k_2)$ is not correlated with other parameters. The log-likelihood function is used to explore the
493 parameter space and determine the posterior distribution of internal structure model parameters. We also compute the libration
494 amplitude γ for each step in the Markov chain. The posterior distribution of γ is shown in Extended Data Fig. 4. There is an
495 overlap between the two probability distributions, but smaller libration amplitudes are possible for the no magma ocean case.
496 Full posterior distributions are shown in Extended Data Fig. 5 and Extended Data Fig. 6.

497 Physical libration introduces an apparent time-variability of S_{22} . The amplitude of this variation is δS_{22} , which we refer to as
498 gravitational libration amplitude. S_{22} varies with respect to uniform rotation due to the periodic oscillation of the outer solid
499 shell and, in the magma ocean case, also the inner solid mantle. The shapes of the interfaces are assumed hydrostatic in our
500 modeling. The posterior distributions for the linear and gravitational libration amplitudes are shown in Extended Data Fig. 7.
501 For the no magma ocean case, there is nearly one-to-one correspondence between the two libration amplitudes. However, a
502 wider range of libration amplitude combinations is possible if a magma ocean is present. Gravitational libration amplitudes are
503 typically lower for the case with a magma ocean. Since the overlap between the two posterior distributions is minimal, future
504 simultaneous measurements of the gravitational and linear libration amplitudes can be used to rule out even a deep magma
505 ocean.

506 **Thickness of Io's Rigid Lid**

507 A rigid lid or elastic lithosphere of some thickness is necessary to support Io's more than 100 towering mountains, some of
508 which reach elevations 17 km above Io's background plains⁷⁵. These are widely interpreted as a product of Io's heat-pipe
509 volcanic cycle. In this Io's copious volcanism reaches the surface through discrete conduits, but the continuous resurfacing
510 causes downward advection of the cooled surface layers and increasing lateral compression at depth. This downward advection
511 strongly suppresses radially outward heat conduction, away from volcanic centers⁸¹, stabilizing the required elastic lithosphere.
512 Increasing compression eventually causes brittle failure at depth, forming thrust faults, which propagate upward through the
513 lithosphere and breach the surface, creating the mountains⁸². These tectonic mountains themselves constrain the thickness of
514 the elastic lithosphere that supports them. The minimum estimated thickness d is given by the tallest mountains (17 km).
515 Mountains on Io are spaced on average about 600 km apart. If we suppose that all mountains initially form 10 km high, which
516 implies approximately 15 km of horizontal displacement along a 30° inclined thrust ramp, then the horizontal strain implied is
517 about $15/600 = 2.5\%$. This amount of horizontal strain is reached when a surface layer on Io is driven downward by 46 km \approx
518 50 km. A similar estimate of $d \lesssim 50$ km was obtained previously⁸³ by summing up the total volume of Io's mountains today
519 and equating it to the volumetric strain at depth due to faulting.

520
521
522

523

Data availability

524 The Juno radio science data used in this research are publicly available through NASA's Planetary Data System at
525 https://atmos.nmsu.edu/PDS/data/jnogr1_1001/. Partial Galileo data are available through the NASA Planetary Data System at
526 <https://pds-ppi.igpp.ucla.edu/>.

527

528

Code availability

529 The results presented in this study can be reproduced using the MONTE software. The license for MONTE can be requested
530 through montepy.jpl.nasa.gov. The code that can reproduce our MCMC results is available on Zenodo:
531 [10.5281/zenodo.14029354](https://zenodo.org/record/10.5281/zenodo.14029354).

532 **References for Methods**

533

534 52 Geissler, P. E. *et al.* Global Color Variations on Io. *Icarus* **140**, 265-282 (1999).
<https://doi.org/https://doi.org/10.1006/icar.1999.6128>

535

536 53 Gomez Casajus, L. *et al.* Gravity Field of Ganymede After the Extended Mission. *Geophys Res Lett* **49** (2022).
<https://doi.org/10.1029/2022GL099475>

537

538 54 Bagenal, F. Empirical-Model of the Io Plasma Torus - Voyager Measurements. *J Geophys Res-Space* **99**, 11043-11062 (1994). <https://doi.org/10.1029/93ja02908>

539

540 55 Bertotti, B., Comoretto, G. & Iess, L. Doppler Tracking of Spacecraft with Multifrequency Links. *Astron Astrophys* **269**, 608-616 (1993).

541

542 56 Mariotti, G. & Tortora, P. Experimental validation of a dual uplink multifrequency dispersive noise calibration scheme for Deep Space tracking. *Radio Sci* **48**, 111-117 (2013). <https://doi.org/10.1002/rds.20024>

543

544 57 Moirano, A., Casajus, L. G., Zannoni, M., Durante, D. & Tortora, P. Morphology of the Io Plasma Torus From Juno Radio Occultations. *J Geophys Res-Space* **126** (2021). <https://doi.org/10.1029/2021JA029190>

545

546 58 Phipps, P. H., Withers, P., Buccino, D. R., Yang, Y. M. & Parisi, M. Two Years of Observations of the Io Plasma Torus by Juno Radio Occultations: Results From Perijoves 1 to 15. *J Geophys Res-Space* **126** (2021).
<https://doi.org/10.1029/2020JA028710>

547

548 59 Gurnett, D. A., Kurth, W. S., Roux, A., Bolton, S. J. & Kennel, C. F. Galileo plasma wave observations in the Io plasma torus and near Io. *Science* **274**, 391-392 (1996). <https://doi.org/10.1126/science.274.5286.391>

549

550 60 Phipps, P. H., Withers, P., Buccino, D. R. & Yang, Y. M. Distribution of Plasma in the Io Plasma Torus as Seen by Radio Occultation During Perijove 1. *J Geophys Res-Space* **123**, 6207-6222 (2018).
<https://doi.org/10.1029/2017ja025113>

551

552

553 61 Heiskanen, W. A. & Moritz, H. *Physical Geodesy*. (W. H. Freeman and Company, 1967).

554 62 Park, R. S. *et al.* Evidence of non-uniform crust of Ceres from Dawn's high-resolution gravity data. *Nat Astron* **4**, 748-755 (2020). <https://doi.org/10.1038/s41550-020-1019-1>

555

556 63 Love, A. E. H. *A Treatise on the Mathematical Theory of Elasticity*. (Cambridge Univ. Press, 1927).

557 64 Munk, W. H. & MacDonald, G. J. F. *The Rotation of the Earth*. (Cambridge Univ. Press, 1960).

558

559 65 Park, R. S. *et al.* Detecting tides and gravity at Europa from multiple close flybys. *Geophys Res Lett* **38** (2011).
<https://doi.org/10.1029/2011gl049842>

560

561 66 Park, R. S. *et al.* Improved detection of tides at Europa with radiometric and optical tracking during flybys. *Planet Space Sci* **112**, 10-14 (2015). <https://doi.org/10.1016/j.pss.2015.04.005>

562

563 67 Greenberg, R. & Weidenschilling, S. J. How fast do Galilean satellites spin? *Icarus* **58**, 186-196 (1984).
[https://doi.org/https://doi.org/10.1016/0019-1035\(84\)90038-1](https://doi.org/https://doi.org/10.1016/0019-1035(84)90038-1)

564

565 68 Makarov, V. V. & Efroimsky, M. No Pseudosynchronous Rotation for Terrestrial Planets and Moons. *Astrophys J* **764** (2013). <https://doi.org/10.1088/0004-637x/764/1/27>

566

567 69 Lainey, V. *et al.* Interior properties of the inner saturnian moons from space astrometry data. *Icarus* **326**, 48-62 (2019). <https://doi.org/10.1016/j.icarus.2019.01.026>

568

569 70 Park, R. S. *et al.* The Global Shape, Gravity Field, and Libration of Enceladus. *J Geophys Res-Planet* **129** (2024).
<https://doi.org/10.1029/2023JE008054>

570

571 71 Jacobson, R. A. & Park, R. S. in *European Planetary Science Congress*.

572 72 Efroimsky, M. & Makarov, V. V. Tidal Friction and Tidal Lagging. Applicability Limitations of a Popular Formula for the Tidal Torque. *Astrophys J* **764** (2013). <https://doi.org/10.1088/0004-637x/764/1/26>

573

574 73 Jacobson, R. A. The Orbits of the Main Saturnian Satellites, the Saturnian System Gravity Field, and the Orientation of Saturn's Pole*. *Astron J* **164** (2022). <https://doi.org/10.3847/1538-3881/ac90c9>

575

576 74 Park, R. S., Folkner, W. M., Williams, J. G. & Boggs, D. H. The JPL Planetary and Lunar Ephemerides DE440 and DE441. *Astron J* **161** (2021). <https://doi.org/10.3847/1538-3881/abd414>

577

578 75 Turtle, E. P., Jaeger, W. L. & Schenk, P. M. in *Io After Galileo: A New View of Jupiter's Volcanic Moon* (eds Rosaly M. C. Lopes & John R. Spencer) 109-131 (Springer Berlin Heidelberg, 2007).

579

580 76 Kervazo, M., Tobie, G., Choblet, G., Dumoulin, C. & Behounková, M. Inferring Io's interior from tidal monitoring. *Icarus* **373** (2022). <https://doi.org/10.1016/j.icarus.2021.114737>

581

582 77 Kamata, S., Matsuyama, I. & Nimmo, F. Tidal resonance in icy satellites with subsurface oceans. *J Geophys Res-Planet* **120**, 1528-1542 (2015). <https://doi.org/10.1002/2015je004821>

583

584 78 Takeuchi, H. & Saito, M. in *Methods in Computational Physics: Advances in Research and Applications* Vol. 11 (ed Bruce A. Bolt) 217-295 (Elsevier, 1972).

585

586 79 Van Hoolst, T., Baland, R. M. & Trinh, A. On the librations and tides of large icy satellites. *Icarus* **226**, 299-315 (2013). <https://doi.org/10.1016/j.icarus.2013.05.036>

587

588 80 Foreman-Mackey, D., Hogg, D. W., Lang, D. & Goodman, J. emcee: The MCMC Hammer. *Publ Astron Soc Pac* **125**, 306-312 (2013). <https://doi.org/10.1086/670067>

590 81 Oreilly, T. C. & Davies, G. F. Magma Transport of Heat on Io - a Mechanism Allowing a Thick Lithosphere.
591 82 *Geophys Res Lett* **8**, 313-316 (1981). <https://doi.org/10.1029/GL008i004p00313>

592 82 Bland, M. T. & McKinnon, W. B. Mountain building on Io driven by deep faulting. *Nat Geosci* **9**, 429-+ (2016).
593 82 <https://doi.org/10.1038/Ngeo2711>

594 83 Jaeger, W. L., Turtle, E. P., Keszthelyi, L. P., Radebaugh, J. & McEwen, A. S. Orogenic tectonism on Io. *J Geophys
595 83 Res-Planet* **108** (2003). <https://doi.org/10.1029/2002je001946>

596

ACCELERATED ARTICLE PREVIEW

597
598
599
600
601
602
603

Acknowledgements

This research was carried out in part at the Jet Propulsion Laboratory, California Institute of Technology, under a contract with the National Aeronautics and Space Administration. All rights reserved. Special thanks to Dr. William Folkner and Dr. Alexander Konopliv for providing helpful comments and suggestions, as well as inspiring guidance throughout this endeavor. All the authors thank the Juno flight team for providing invaluable science and engineering data that facilitated the successful gravity science investigation of Io, with special thanks to the Juno navigation team for the safe and precise flybys of Io.

604

Author information

605

606

Authors and Affiliations

607

Jet Propulsion Laboratory, California Institute of Technology, Pasadena, California, USA

608

R. S. Park, R. A. Jacobson, J. T. Keane, D. R. Buccino, M. Parisi, S. M. Levin

609

610

Centro Interdipartimentale di Ricerca Industriale Aerospaziale, Alma Mater Studiorum - Università di Bologna, Forlì, Italy

611

L. Gomez Casajus

612

613

Department of Earth and Planetary Sciences, University of California, Santa Cruz, California, USA

614

F. Nimmo, R. Akiba, B. Idini

615

616

Department of Aeronautics and Astronautics, Stanford University, Stanford, California, USA

617

A. I. Ermakov

618

619

Department of Earth, Environmental, and Planetary Sciences, Washington University, St. Louis, Missouri, USA

620

W. B. McKinnon

621

622

California Institute of Technology, Pasadena, California, USA

623

D. J. Stevenson

624

625

Dipartimento di Ingegneria Industriale, Alma Mater Studiorum, Università di Bologna, Forlì, Italy

626

A. Magnanini, P. Tortora, M. Zannoni

627

628

Institute for Space Astrophysics and Planetology, National Institute for Astrophysics, 00133 Rome, Italy

629

A. Mura

630

631

Sapienza Università di Roma, 00184 Rome, Italy

632

D. Durante, L. Iess

633

634

NASA Goddard Space Flight Center, Greenbelt, Maryland, USA

635

J. E. P. Connerney

636

637

Southwest Research Institute, San Antonio, Texas, USA

638

S. J. Bolton

639

640

Contributions

641

642

R.S.P led the experiment and supervised the data analysis. R.S.P., R.A.J., L.G.C., A.Ma, P.T., and M.Z. contributed to the orbit determination and recovery of the Io gravity parameters. L.G.C., D.R.B., and M.P. contributed to data calibration and conditioning. R.S.P., F.N., A.I.E., J.T.K., W.B.M., D.J.S., R.A, B.I., A.Mu, D.D., and L.I. contributed to interior modeling and interpretation of the Io gravity results. A.I.E., R.A, and F.N. contributed to the statistical analysis of interior modeling. J.E.P.C., S.M.L., and S.J.B. supervised the planning and execution of the gravity experiment. All authors contributed to the discussion of the results and to writing the paper.

643

644

645

646

647

648

649

Competing interests

650

The authors declare no competing interests.

651

652

Corresponding author

653

Correspondence to Ryan S. Park (ryan.s.park@jpl.nasa.gov)

654

655
656
657
658
659
660
661

Extended Data Figure/Table legends

662 **Extended Data Fig. 1 | Ground tracks of Galileo (I24, I25, I27, I32, and I33) and Juno (I57 and I58) for altitude $\leq 5,000$ km of the closest approach over a color image mosaic of Io⁵².** The altitudes were computed relative to a spherical Io, assuming an 1829.4-km radius. The black circles represent the closest approaches. The angles in the parenthesis represent the true anomaly of Io with respect to Jupiter.

663 **Extended Data Fig. 2 | Doppler residuals of Galileo (I24, I25, I27, I32, and I33) and Juno (I57 and I58) near the closest approach to Io.** The black vertical lines represent the time of the closest approach. The Doppler rms for each flyby is shown in the upper right side of each plot. The red-dashed and cyan-dotted lines represent the $\pm 1\sigma$ and $\pm 3\sigma$ ranges of the Doppler rms, respectively. Nearly all points are well within the 3σ range. The Juno Doppler data is generally about an order of magnitude more accurate than the Galileo Doppler data (note the scale of the axes).

664 **Extended Data Fig. 3 | Effect of solid core and 50 km thick elastic lid on tidal response.** a) Effect of a solid core on the no magma ocean case. Solid and dashed lines represent cases with a liquid and solid core, respectively. The solid core case results in a lower $\text{Re}(k_2)$ for a given mantle rheology. b) Effect of adding a 50 km thick elastic lid to the case with a magma ocean (i.e., a 5-layer case). Solid and dashed lines represent cases without and with an elastic lid, respectively.

665 **Extended Data Fig. 4 | Posterior distribution of the upper mantle thickness and physical libration amplitude.** a) Posterior distribution of the upper mantle thickness for the case with a magma ocean. The upper mantle thickness h represents the depth to the top of the global magma ocean layer. The median value of h is 605 km. The vertical dashed lines indicate 5th and 95th percentiles that correspond to thicknesses of 420 km and 810 km, respectively. At a 3σ level (0.135% probability), the lower bound on the upper mantle thickness is 318 km, b) Posterior distribution of the physical libration amplitude for the cases with and without a magma ocean. The “with magma ocean” case represents the distribution of solutions with a magma ocean, whose depth is constrained by the observed static gravity and Love numbers. Although the two probability distributions overlap, smaller libration amplitudes are possible for the no magma ocean case, indicating that future measurements of libration could exclude the deep magma ocean case.

666 **Extended Data Fig. 5 | Corner plot showing the posterior distribution of Io’s internal structure parameters for the case with a magma ocean.** The variables are named as follows: h_i are layer thicknesses, ρ_i are layer densities, δC_{nm} are non-hydrostatic contributions to gravity coefficients C_{nm} , μ_i are shear moduli, η_i are viscosities, β_i are the Andrade rheology parameters. The layers are numbered from the outermost layer inward.

667 **Extended Data Fig. 6 | Corner plot showing the posterior distribution of Io’s internal structure parameters for the case without a magma ocean.** The variables are named as follows: h_i are layer thicknesses, ρ_i are layer densities, δC_{nm} are non-hydrostatic contributions to gravity coefficients C_{nm} , μ_i are shear moduli, η_i are viscosities, β_i are the Andrade rheology parameters. The layers are numbered from the outermost layer inward.

668 **Extended Data Fig. 7 | Posterior distribution of gravitational and linear libration amplitudes for the cases with and without a magma ocean.** The vertical axis shows the gravitational libration amplitude and the horizontal axis shows the libration amplitude (with 1σ , 2σ and 3σ regions are shown).

669 **Extended Data Table 1 | Recovered Io quadrupole gravity field and the tidal Love number k_2 .** The spherical harmonic coefficients are un-normalized and uncertainties are formal 1σ . The reference radii used in some of the earlier analyses differ from ours; thus, the quadrupole harmonic values in this table have all been adjusted to the same reference radius of 1829.4 km. In our estimation, the dissipation quality factor is directly estimated $Q=11.4\pm 3.6$ (1σ) and combined with $|k_2|$ to compute the ratio $|k_2|/Q=-\text{Im}(k_2)$. Our estimated μ_i is 5959.8948 ± 0.0027 km^3/s^2 (1σ). The correlations between $\text{Re}(k_2)$ and permanent tide correlated J_2 and C_{22} are 0.0291 and 0.5120, respectively, while the correlation between permanent tide correlated J_2 and C_{22} is 0.0026.

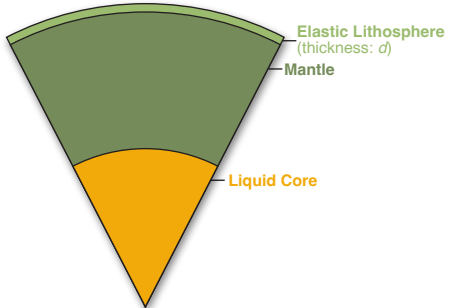
670 **Extended Data Table 2 | Tabulation of model parameters for no-magma ocean and magma ocean cases** (see text). “Var.” means “variable”. Our default magma ocean thickness is 100 km.

671 **Extended Data Table 3 | Full model input for the magma ocean case.** Parameters of the prior probability distribution for the internal structure retrieval of the four-layer modeling including a magma ocean.

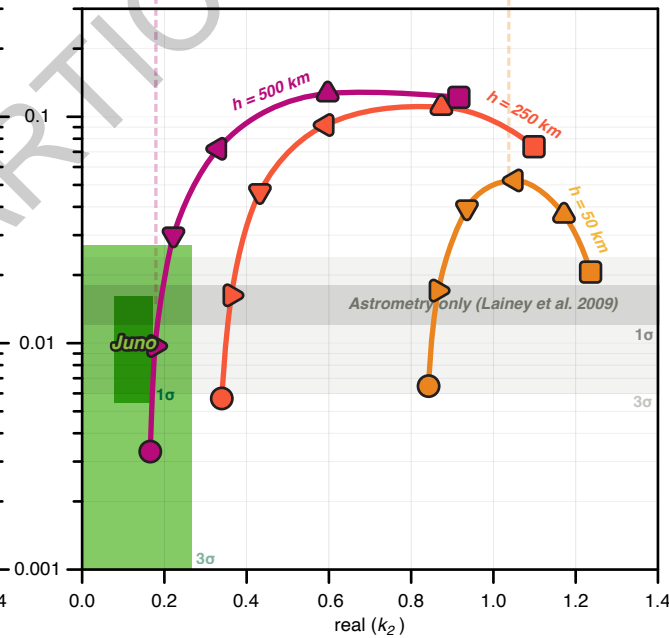
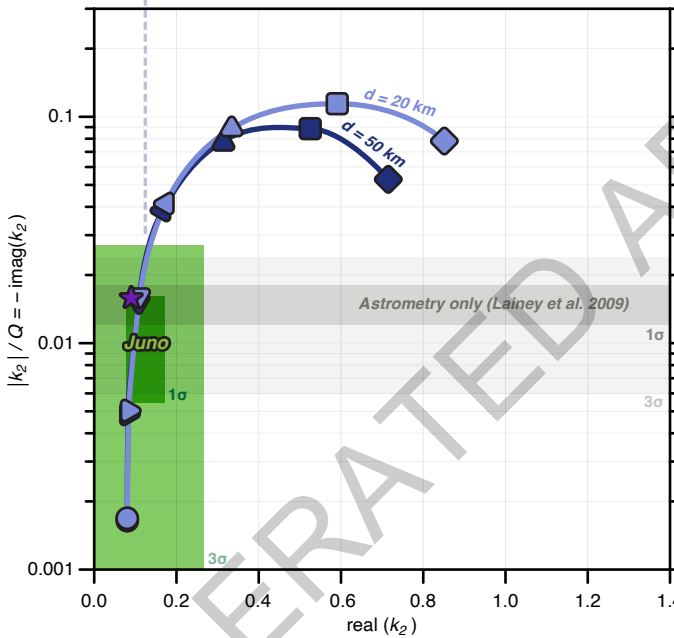
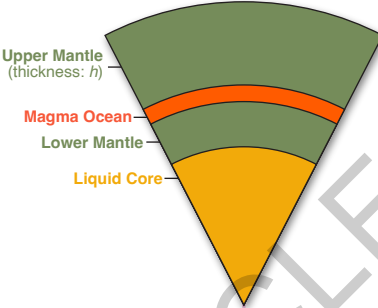
711 **Extended Data Table 4 | Full model input for the no magma ocean case.** Parameters of the prior probability distribution for
712 the internal structure retrieval of the three-layer modeling without a magma ocean.

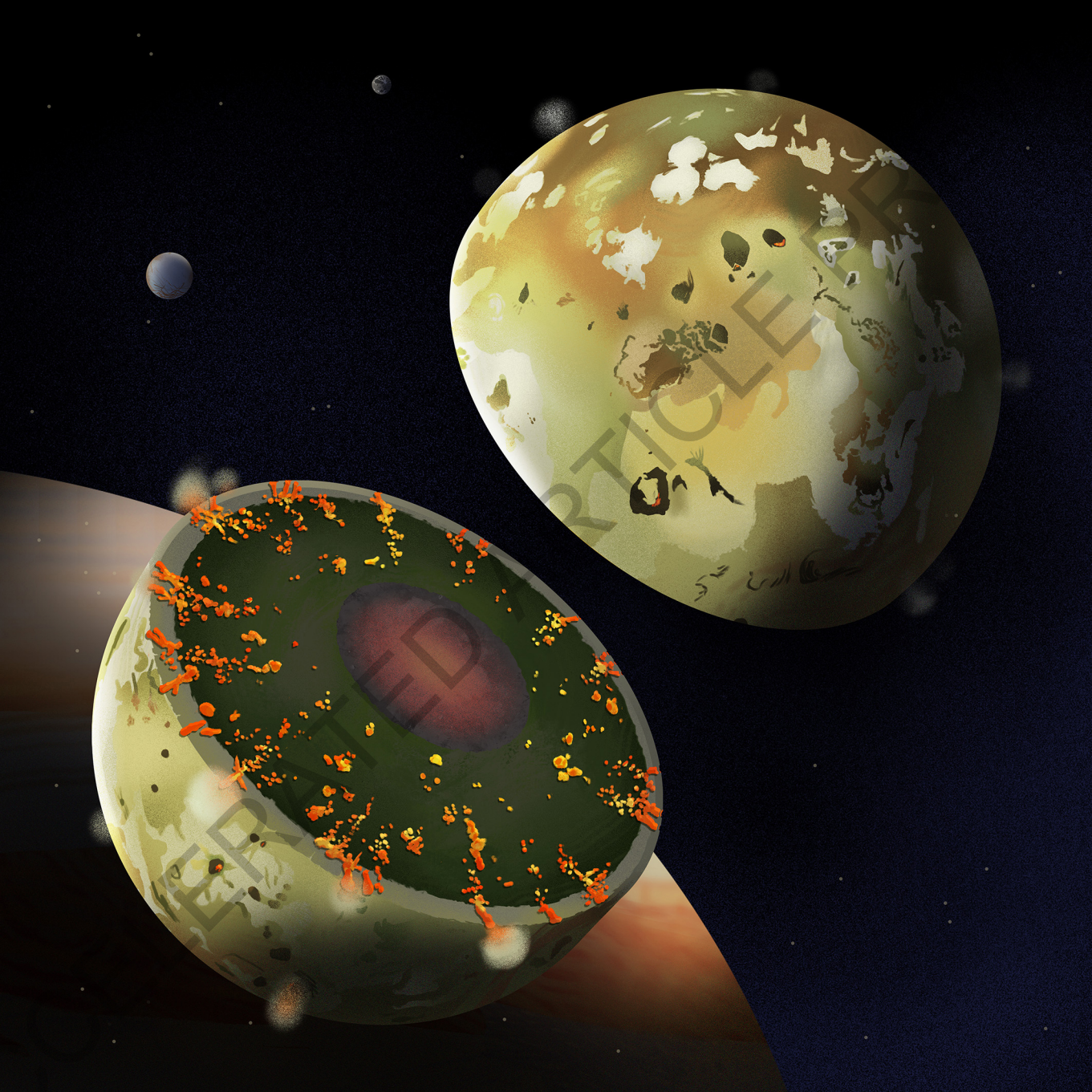
ACCELERATED ARTICLE PREVIEW

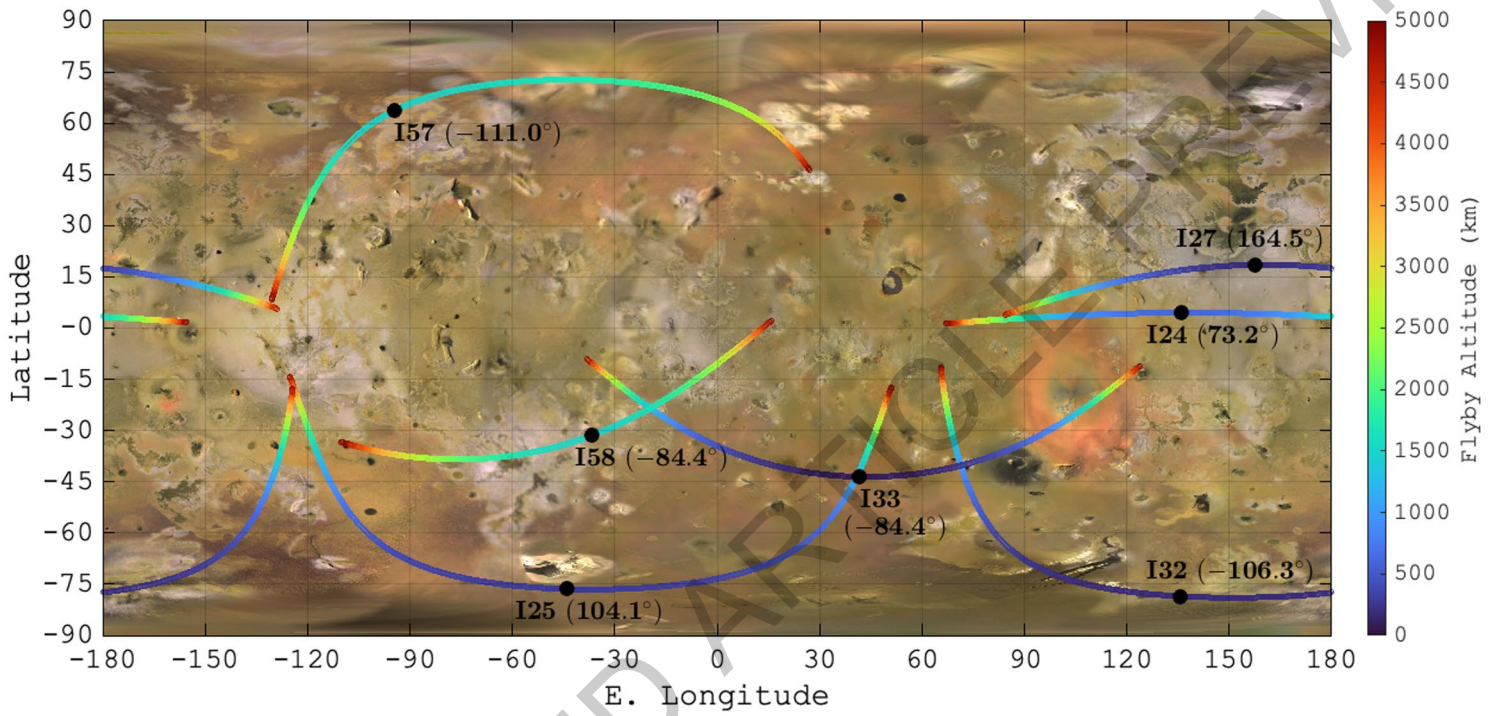
a — Tidal response of Io without a magma ocean



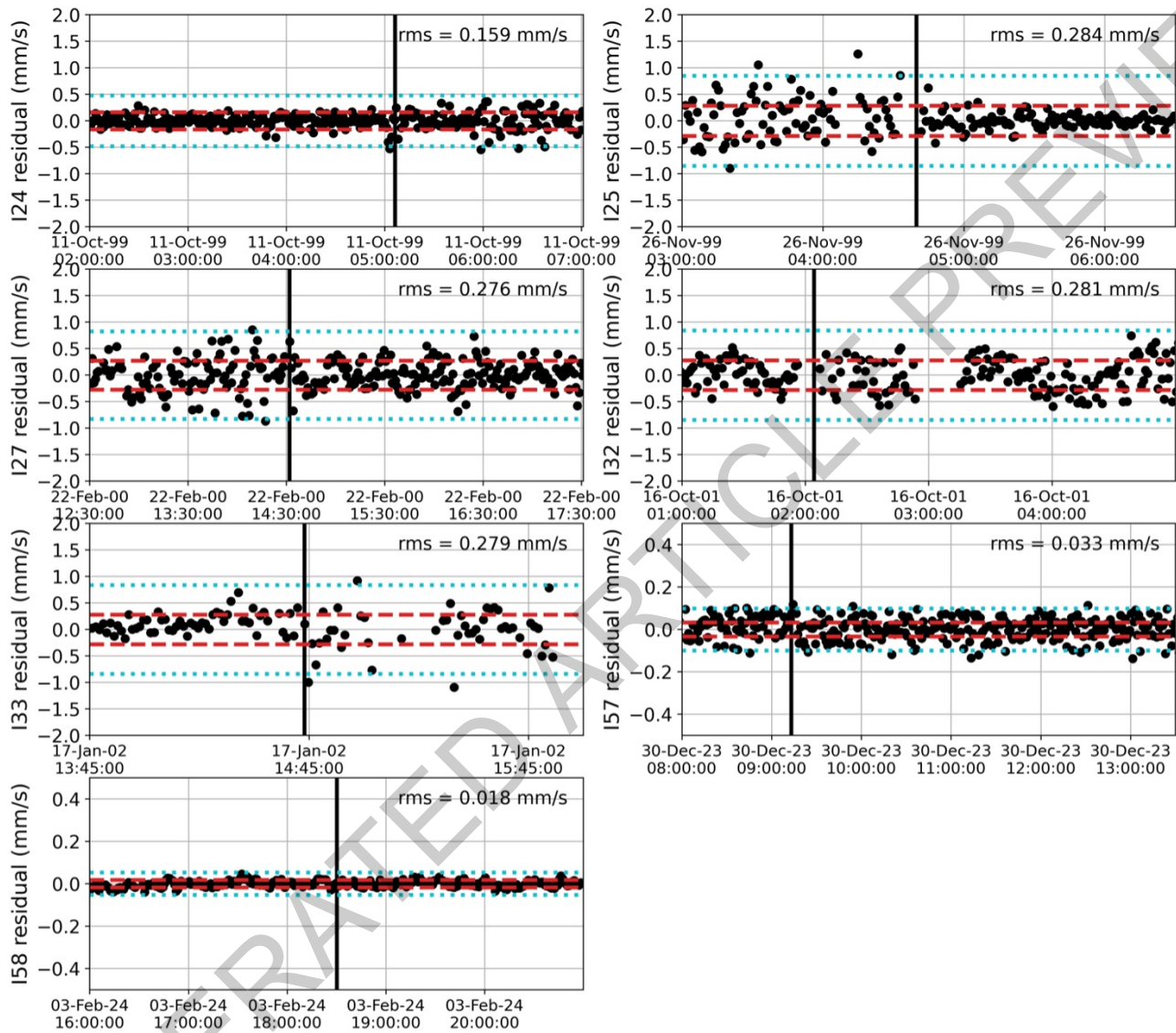
b — Tidal response of Io with a magma ocean



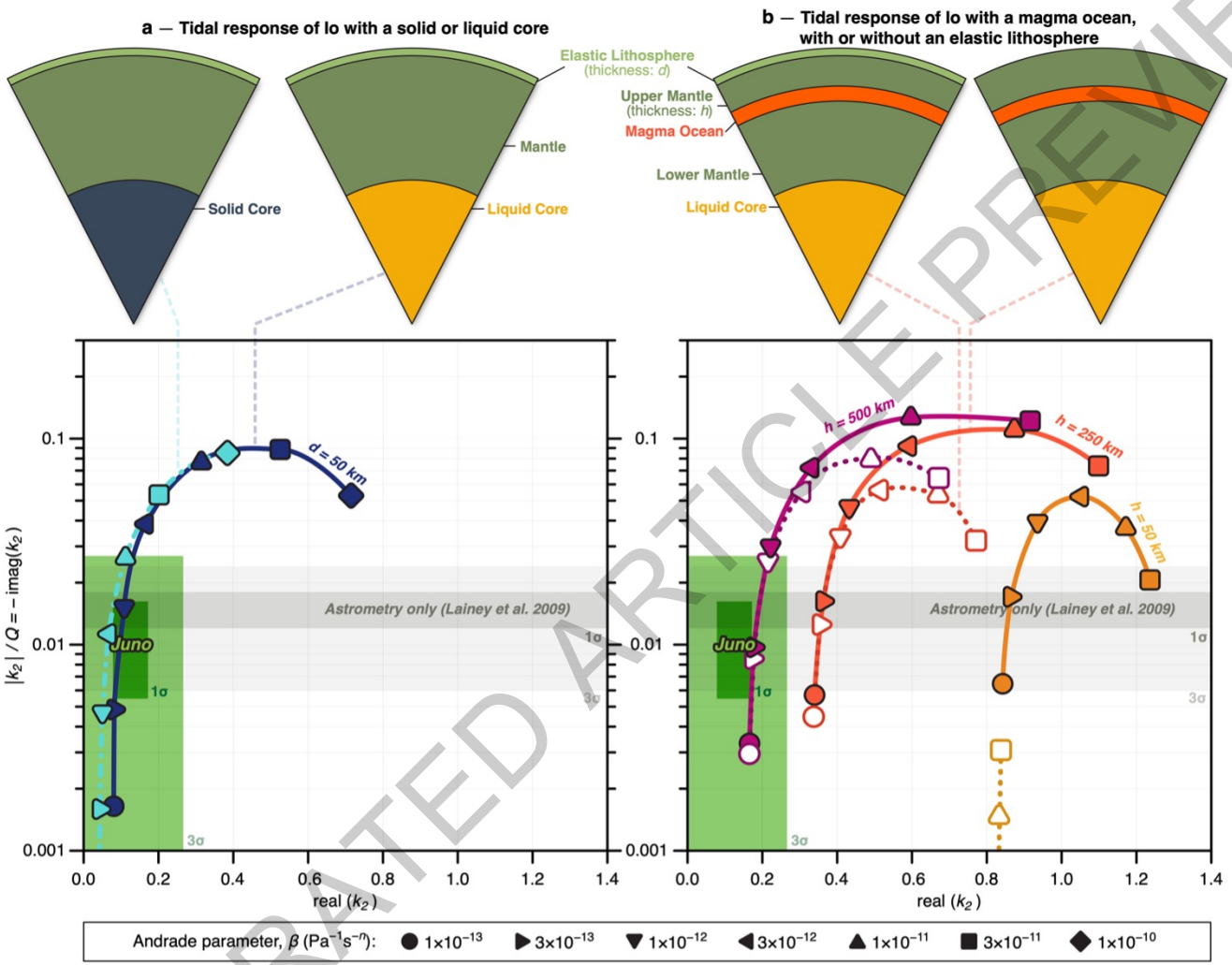




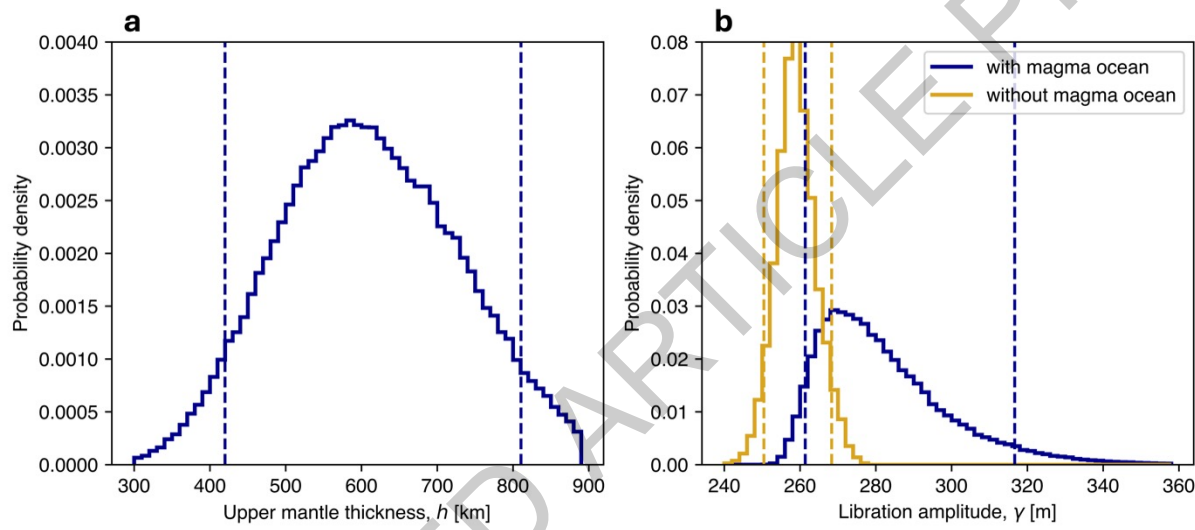
Extended Data Fig. 1



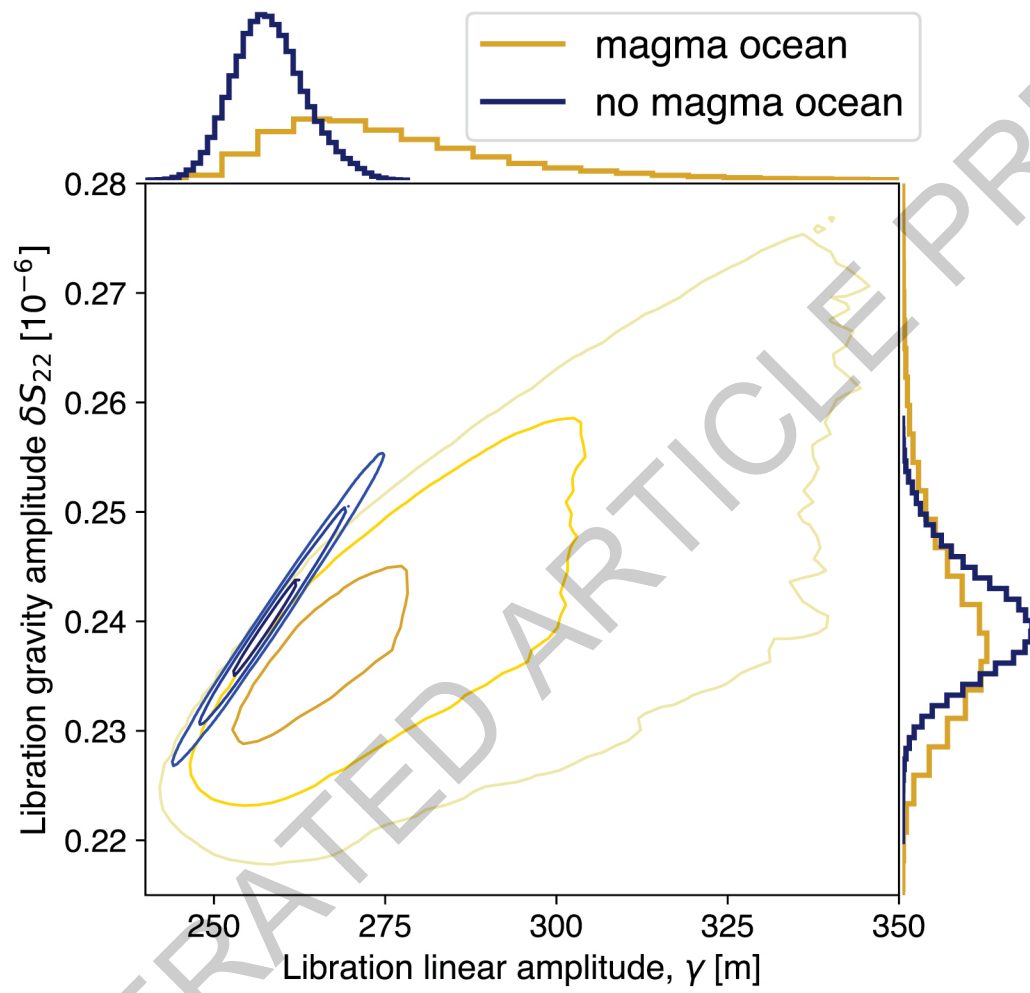
Extended Data Fig. 2

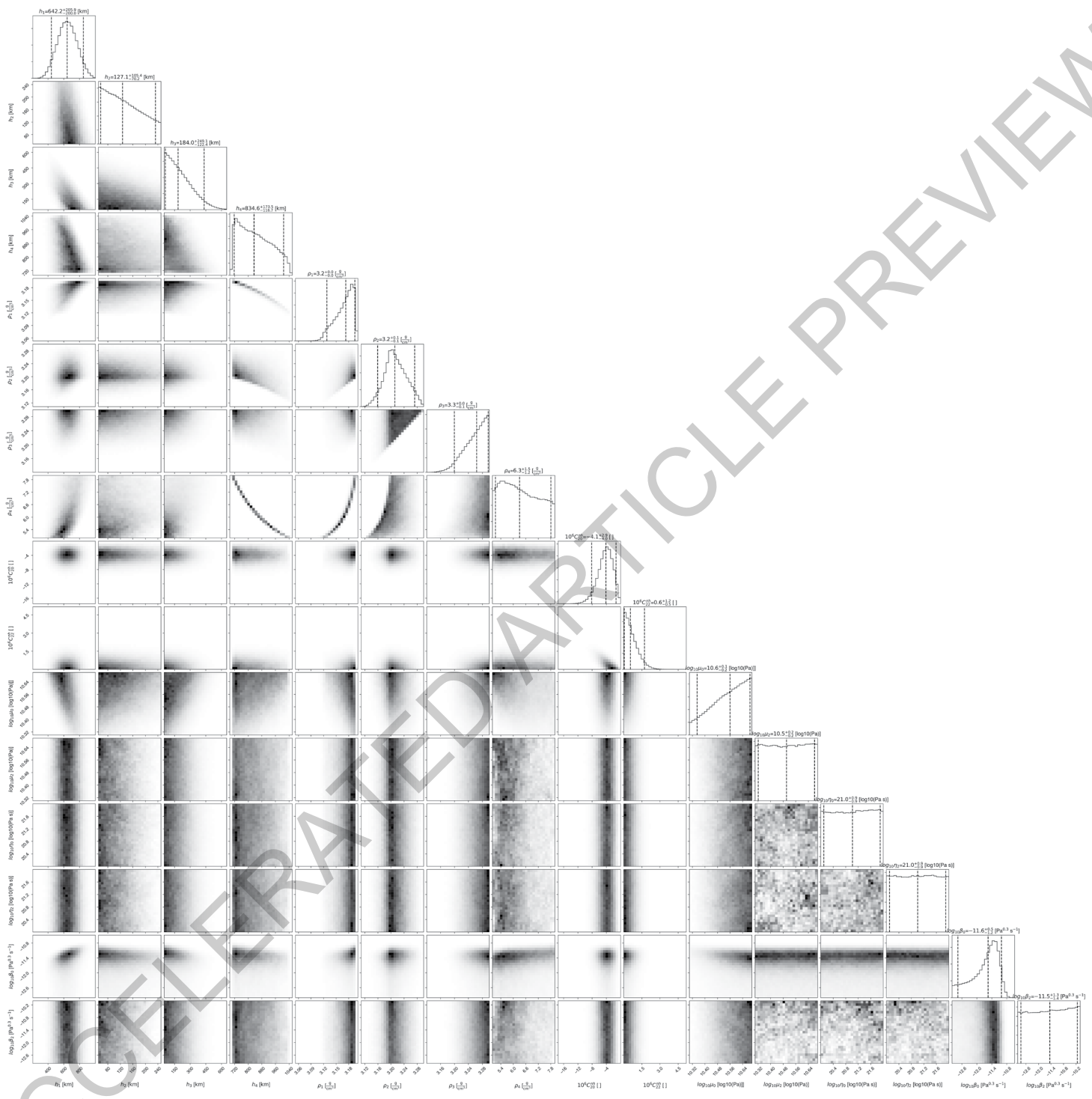


Extended Data Fig. 3

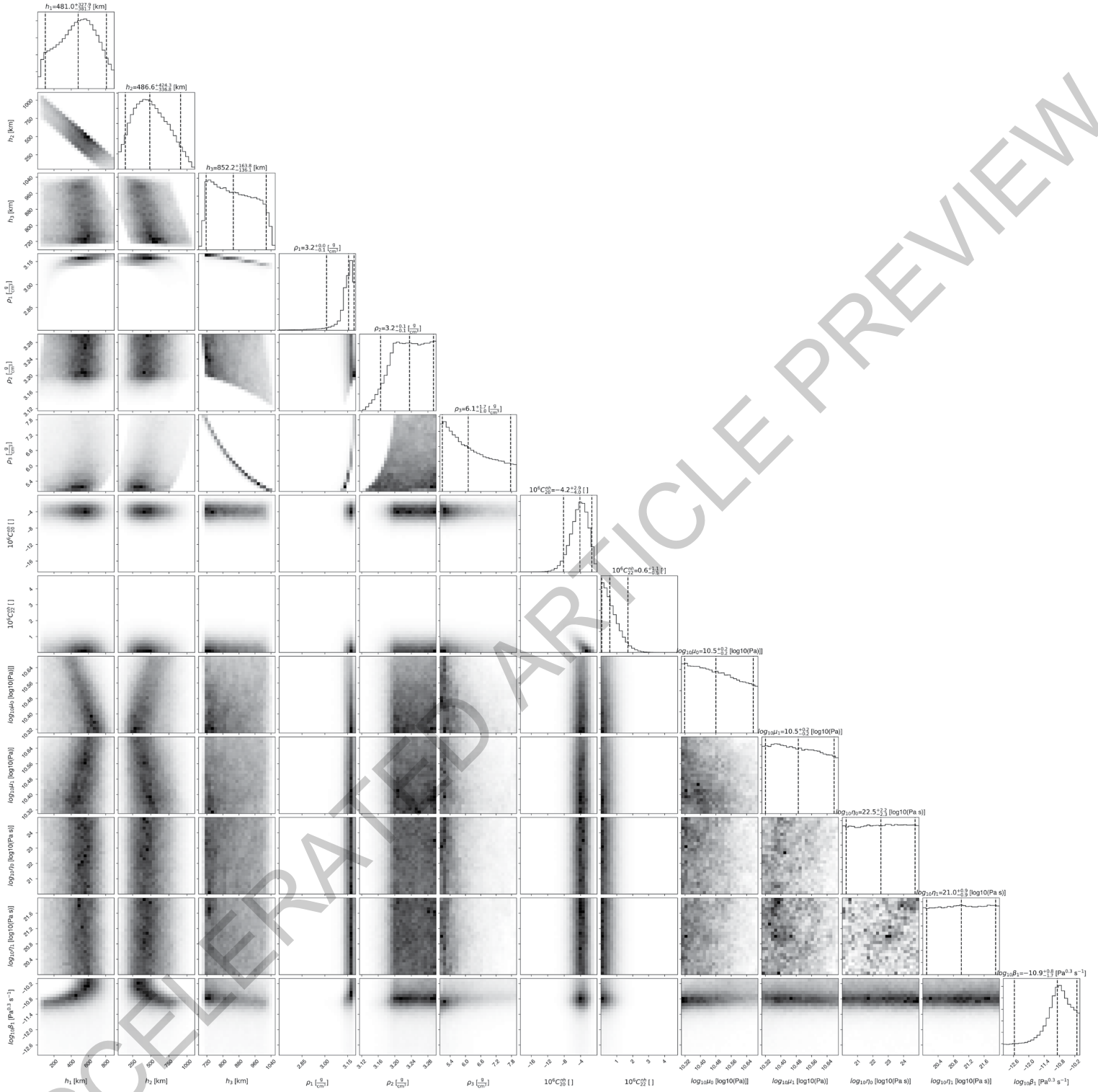


Extended Data Fig. 4





Extended Data Fig. 6



$J_2 (10^6)$	$C_{21} (10^6)$	$S_{21} (10^6)$	$C_{22} (10^6)$	$S_{22} (10^6)$	$Re(k_2)$	$\frac{ k_2 }{Q} = -Im(k_2)$	Notes
1863.0 ± 90.0	-	-	559.0 ± 27.0	-	-	-	Anderson et al. (1996)
1830.2 ± 4.2	-	-	548.9 ± 1.2	-	-	-	Anderson et al. (2001)
1843.7 ± 2.7	-	-	554.0 ± 0.8	-	-	-	Schubert et al. (2004)
-	-	-	-	-	-	0.015 ± 0.003	Lainey et al. (2009)
1834.6 ± 1.5 (108.4)	0.0 ± 0.1	-4.0 ± 0.8	549.6 ± 0.3 (54.0)	0.5 ± 0.3 (4.6)	0.125 ± 0.047	0.0109 ± 0.0054	This study (includes the permanent tide corrections from k_2 and lag angle shown in the parenthesis).

Extended Data Table 1

No magma ocean case						Magma ocean case					
	Outer radius (km)	Density (kg m ⁻³)	Rigidity (GPa)	Steady-state viscosity (Pa s)	Andrade parameter β (Pa ^{-0.3} s ⁻¹)		Outer radius (km)	Density (kg m ⁻³)	Rigidity (GPa)	Steady-state viscosity (Pa s)	Andrade parameter β (Pa ^{-0.3} s ⁻¹)
Core	950	5150	0	0	0	Core	950	5150	0	0	0
Mantle	var.	3259	40	10^{21}	var.	Mantle	var.	3259	40	10^{21}	var.
Lid	1820	3259	40	10^{25}	0	Magma ocean	var. + 100	3259	0.06	10^4	0
						Mantle	1820	3259	40	10^{21}	var.

Extended Data Table 2

Parameter	Minimum value	Maximum value	Type of distribution	Additional constraints
Top mantle outer radius	1820 km	1820 km	constant value	Thickness between 10 and 900 km
Magma ocean outer radius	500 km	1820 km	uniform	Magma ocean thickness between 50 and 1200 km
Bottom mantle outer radius	500 km	1820 km	uniform	Thickness between 50 and 650 km
Core radius	650 km	1200 km	uniform	None
Magma ocean density	2700 kg/m ³	3300 kg/m ³	uniform	Densities are constrained to increase with depth. The density of the top layer is computed to satisfy the mass constraint.
Mantle density	2700 kg/m ³	3300 kg/m ³	uniform	
Core density	5000 kg/m ³	8000 kg/m ³	uniform	
Top mantle shear modulus	30 GPa	50 GPa	log-uniform	None
Bottom mantle shear modulus	30 GPa	50 GPa	log-uniform	None
Top mantle viscosity	10 ²⁰ Pa s	10 ²² Pa s	log-uniform	None
Bottom mantle viscosity	10 ²⁰ Pa s	10 ²² Pa s	log-uniform	None
Top mantle Andrade β parameter	10 ⁻¹³ Pa ^{0.3} s ⁻¹	10 ⁻¹⁰ Pa ^{0.3} s ⁻¹	log-uniform	None
Bottom mantle Andrade β parameter	10 ⁻¹³ Pa ^{0.3} s ⁻¹	10 ⁻¹⁰ Pa ^{0.3} s ⁻¹	log-uniform	None
Nonhydrostatic contribution to C_{20}	$-4\sigma_{nh}$	$+4\sigma_{nh}$	Normal, zero-centered with $\sigma_{20}^{nh} = \sqrt{5} \cdot 2 \cdot 10^{-6}$	Rotational stability is imposed: $C_{22}^{nh} > 0$ $-C_{20}^{nh} > 2C_{22}^{nh}$
Nonhydrostatic contribution to C_{22}	$-4\sigma_{nh}$	$+4\sigma_{nh}$	Normal, zero-centered with $\sigma_{22}^{nh} = \sqrt{5/12} \cdot 2 \cdot 10^{-6}$	

Extended Data Table 3

Parameter	Minimum value	Maximum value	Type of distribution	Additional constraints
Elastic lid outer radius	1820 km	1820 km	constant value	Thickness between 10 and 900 km
Mantle outer radius	500 km	1820 km	uniform	Thickness between 50 and 1200 km
Core radius	650 km	1200 km	uniform	None
Elastic lid density	2700 kg/m ³	3300 kg/m ³	uniform	Densities are constrained to increase with depth. The density of the top layer is computed to satisfy the mass constraint.
Mantle density	2700 kg/m ³	3300 kg/m ³	uniform	
Core density	5000 kg/m ³	8000 kg/m ³	uniform	
Elastic lid shear modulus	20 GPa	50 GPa	log-uniform	None
Mantle shear modulus	20 GPa	50 GPa	log-uniform	None
Mantle viscosity	10 ²⁰ Pa s	10 ²² Pa s	log-uniform	None
Mantle Andrade β parameter	10 ⁻¹³ Pa ^{0.3} s ⁻¹	10 ⁻¹⁰ Pa ^{0.3} s ⁻¹	log-uniform	None
Nonhydrostatic contribution to C_{20}	$-4\sigma_{nh}$	$+4\sigma_{nh}$	Normal, zero-centered with $\sigma_{20}^{nh} = \sqrt{5} \cdot 2 \cdot 10^{-6}$	Rotational stability is imposed: $C_{22}^{nh} > 0$ $-C_{20}^{nh} > 2C_{22}^{nh}$
Nonhydrostatic contribution to C_{22}	$-4\sigma_{nh}$	$+4\sigma_{nh}$	Normal, zero-centered with $\sigma_{22}^{nh} = \sqrt{5/12} \cdot 2 \cdot 10^{-6}$	

Extended Data Table 4